MOLECULAR CLOUD STRUCTURE IN THE MAGELLANIC CLOUDS: EFFECT OF METALLICITY

SOOJONG PAK[1,2] AND D. T. JAFFE[2]
Department of Astronomy, University of Texas, Austin, TX 78712

EWINE F. VAN DISHOECK[3]
Sterrewacht Leiden, P.O. Box 9513, 2300 RA Leiden, The Netherlands

AND

L. E. B. JOHANSSON AND R. S. BOOTH
Onsala Space Observatory, S-439 92 Onsala, Sweden
Received 1997 September 17; accepted 1997 December 23

ABSTRACT

The chemical structure of neutral clouds in low-metallicity environments is examined, with particular emphasis on the H to H_2 and C^+ to CO transitions. We observed near-IR H_2 (1, 0) S(1), (2, 1) S(1), and (5, 3) O(3) lines and the ^{12}CO $J = 1 \rightarrow 0$ line from 30 Doradus and N159/N160 in the Large Magellanic Cloud and from DEM S 16, DEM S 37, and LI-SMC 36 in the Small Magellanic Cloud. We find that the H_2 emission is UV-excited and that (weak) CO emission always exists (in our surveyed regions) toward positions where H_2 and [C II] emission have been detected. Using a PDR code and a radiative transfer code, we simulate the emission of line radiation from spherical clouds and from large planar clouds. Because [C II] emission and H_2 emission arise on the surface of the cloud and because the lines are optically thin, these lines are not affected by changes in the relative sizes of the neutral cloud and the CO-bearing core, while the optically thick CO emission can be strongly affected. The sizes of clouds are estimated by measuring the deviation of CO emission strength from that predicted by a planar cloud model of a given size. The average cloud column density, and therefore its size, increases as the metallicity decreases. Our result agrees with the photoionization-regulated star formation theory of McKee.

Subject headings: ISM: clouds — ISM: structure — radio lines: ISM

1. INTRODUCTION

Stars form in dense, cold molecular clouds. Measuring the molecular gas content of the clouds is very important if we are to estimate the star formation efficiency and relate it to the properties of the clouds and to their environments. The total H_2 mass, however, cannot be measured directly because the lowest levels of H_2 from which the observable emission can arise have excitation energies that are too high (e.g., $\Delta E/k \simeq 500$ K, $J = 2 \rightarrow 0$) to be thermally excited in the cold (< 50 K) molecular clouds. In the Milky Way, the ^{12}CO $J = 1 \rightarrow 0$ line[4] (hereafter CO $J = 1 \rightarrow 0$) traces the molecular gas content. The conversion factor X^{GAL} between the H_2 column density and the velocity-integrated intensity of CO has been measured via the virial theorem ($X^{\text{GAL}} = 2.5$–8×10^{20} cm^{-2} [K km s^{-1}]$^{-1}$; Solomon et al. 1987; Digel et al. 1997 and references therein), or via gamma-ray emission ($X^{\text{GAL}} = 1.1$–2.8×10^{20} cm^{-2} [K km s^{-1}]$^{-1}$; Bloemen et al. 1986; Digel et al. 1997 and references therein). The metallicity dependence of the conversion factor has been an issue. Cohen et al. (1988) and Wilson (1995) used cloud masses determined using the virial theorem to argue that the value of X increases as the metal-

licity of the individual galaxy decreases. Arimoto, Sofue, & Tsujimoto (1996) extend this conclusion to argue that there are radial increases in X in the Milky Way and M51 corresponding to radial decreases in metallicity. In contrast, Taylor, Kobulnicky, & Skillman (1996) showed that some low-abundance galaxies have lower X, suggesting that a factor other than the abundance (e.g., temperature) can affect the measured value of X.

Far-UV photons from massive young stars strike the surfaces of nearby molecular clouds[5] and produce photodissociation regions or photon-dominated regions (hereafter PDRs; Tielens & Hollenbach 1985, 1997). In these surface layers, the far-UV photons dominate the ionization of atoms, the formation and destruction of molecules, and the heating of the gas. Inside the PDR, absorption by dust, C, and H_2 diminishes the far-UV field. Several authors have constructed PDR models appropriate to conditions in the Magellanic Clouds, with particular emphasis on the C^+/C/CO transition (Maloney & Black 1988;[6] van Dishoeck & Black 1988b; Lequeux et al. 1994; Maloney & Wolfire 1997). In irregular galaxies, where metallicities and dust-to-gas ratios are lower than those in the Galaxy, far-UV photons penetrate deeper into clouds and dissociate CO molecules to greater depths (Israel et al. 1986). Therefore, for a cloud with a given column density, the CO column density should be lower at lower metallicity. If the CO column density is high enough for the CO to self-shield against photodissociation [N(CO) $\gtrsim 10^{15}$ cm^{-2};

---

[5] In this paper, "a cloud" implies a UV-illuminated molecular structure either in isolation or in a complex.

[6] Figure 4 in Maloney & Black (1988) is not correct. The figure should be replaced by Figure 2 of Israel (1988) or by Figure 2 of van Dishoeck & Black (1988b).

van Dishoeck & Black 1988a], then the CO column density will also be high enough for the CO $J = 1 \rightarrow 0$ line to be optically thick, and the CO $J = 1 \rightarrow 0$ line intensity ($\int T_{MB} \, dv$) will not depend strongly on the metallicity. In that case, lower CO intensities can only stem from geometrical or beam-filling effects. On the other hand, if the cloud column density is not high, most of the CO will be dissociated and the resulting CO line will be optically thin and very weak. On the surface of the clouds, the destruction and formation of H_2 molecules are also affected by the change of metallicity, but the mechanism is different from that for CO molecules. The H_2 molecules are dissociated by far-UV photons attenuated by dust or by H_2 self-shielding. If H_2 self-shielding dominates over dust attenuation, the H_2 destruction rate is independent of the dust abundance. On the other hand, the H_2 formation rate is proportional to the dust abundance, because H_2 reforms on the surfaces of dust grains.

The Magellanic Clouds are the best targets to test PDR models that include metallicity effects because of their proximity ($d^{LMC} = 50.1$ kpc and $d^{SMC} = 60.3$ kpc; Westerlund 1990), their low metal abundance ($Z_C^{LMC} = 0.28$, $Z_O^{LMC} = 0.54$, $Z_C^{SMC} = 0.050$, and $Z_O^{SMC} = 0.21$, where Z is normalized to the Galactic value; Dufour 1984), and their low dust-to-gas ratio ($\rho_{dust}^{LMC} = 0.25$ and $\rho_{dust}^{SMC} = 0.059$, where ρ is normalized to the Galactic value; Koornneef 1984). In this paper, we observed the Magellanic Clouds in the near-IR H_2 emission lines and in the CO $J = 1 \rightarrow 0$ line (see §§ 2 and 3). We compare the line intensities of H_2 (1, 0) $S(1)$, CO $J = 1 \rightarrow 0$, and [C II] 158 μm emission from the PDRs in the Magellanic Clouds with those from Galactic star formation regions (see § 4). Section 5 discusses the numerical PDR models that we compare to the observed data to learn how metallicity changes affect the chemical structure of the Galactic clouds and the clouds in the Magellanic Clouds.

2. OBSERVATIONS

Some limited regions in the Magellanic Clouds have previously been observed in the H_2 lines (Koornneef & Israel 1985; Israel & Koornneef 1988; Kawara, Nishida, & Taniguchi 1988; Israel & Koornneef 1992; Krabbe et al. 1991; Poglitsch et al. 1995). However, the published [C II] and CO data (Johansson et at. 1994; Poglitsch et al. 1995; Israel et al. 1996) cover more extended regions than the existing H_2 maps. We observed near-IR H_2 emission lines from the Magellanic Clouds with the University of Texas Near-IR Fabry-Perot Spectrometer, with an equivalent-disk size[7] of ($\theta_{ED} = 81''$), comparable to those of the existing [C II] data ($\theta_{ED} = 68''$) and CO $J = 1 \rightarrow 0$ data ($\theta_{ED} = 54''$). We also observed CO $J = 1 \rightarrow 0$ emission at positions where no emission had been detected at the sensitivity of the existing CO surveys.

2.1. Near-IR H_2 Emission Lines

We observed the H_2 (1, 0) $S(1)$ and (2, 1) $S(1)$ lines in 1994 December and the (1, 0) $S(1)$ and (5, 3) $O(3)$ lines in 1995 October at the Cerro Tololo Inter-American Observatory 1.5 m telescope, using the University of Texas Near-Infrared Fabry-Perot Spectrometer (UT FPS; Luhman et al. 1995). The instrument was designed to observe extended, low

surface brightness line emission, and has a single 1 mm diameter InSb detector, to maximize the area–solid angle product. This product, $A\Omega$, depends on the telescope coupling optics but can be made as large as 4.5×10^{-3} cm^2 sr. The beam from the $f/30$ secondary of the telescope is collimated and guided to an H- or K-band Fabry-Perot interferometer and to a ~ 55 K (solid nitrogen temperature) Dewar in which a doublet camera lens (focal length = 20 mm) focuses onto the detector. A 0.5% [for the H_2 (5, 3) $O(3)$ line] or a 1% [for the H_2 (1, 0) $S(1)$ and (2, 1) $S(1)$ lines] interference filter in the Dewar selects a single order from the Fabry-Perot interferometer. We used a collimator of focal length = 838 mm in the 1994 December run and a collimator of focal length = 686 mm in 1995 October. The change of the collimator affected the beam size and spectral resolution (see Table 1). Since the coupling of the 686 mm collimator with the telescope optics is better, the beam profile in 1995 October is much closer to a box function than the 1994 December beam profile (Fig. 1).

An automatic alignment routine aligned the Fabry-Perot etalon by executing every 5–8 minutes (Luhman et al. 1995). The Fabry-Perot etalon maintained alignment for 15–30 minutes, but the ambient temperature changes caused the plate separation to drift by the equivalent of 2–5 km s^{-1} per minute. Using telluric OH lines (Oliva & Origlia 1992), we calibrated the wavelength scale to within ± 30 km s^{-1}.

We operated the Fabry-Perot interferometer in scanning mode at selected positions and in frequency switching mode at most positions. In the scanning mode, the plate separation of the etalon was varied to cover ± 200 km s^{-1} centered at the H_2 line in 15 sequential steps. Figure 2 shows observed H_2 (1, 0) $S(1)$ and (5, 3) $O(3)$ lines at the 30 Doradus (0, 0) position (see the object list in Table 3), and telluric OH lines. The OH (9, 7) $R_2(2)$ ($\lambda = 2.12267$ μm, wavelength in air; Oliva & Origlia 1992) and the (9, 7) $R_1(1)$ ($\lambda = 2.12440$ μm) lines are within the H_2 (1, 0) $S(1)$ scan range. Figure 2 shows the red wing of the OH (4, 2) $P_1(3)$ ($\lambda = 1.61242$ μm) line and the OH (4, 2) $P_1(2)$ ($\lambda = 1.60264$ μm) line, which was displaced by one free spectral range and penetrated through the blue side of the order sorting filter at $V_{LSR} \simeq 420$ km s^{-1}. The typical intensity of the OH (4, 2) $P_1(3)$ and (4, 2) $P_1(2)$ lines is $\sim 4 \times 10^{-3}$ ergs s^{-1} cm^{-2} sr^{-1}, more than 10^3 times the H_2 (5, 3) $O(3)$ intensity.

The OH intensity fluctuates spatially and temporally. The $1/f$ power spectrum of the temporal fluctuations limits the sensitivity of the system, e.g., in the K band, the OH noise becomes important at 30 s (coadded integration time) per step when the switching interval between the source position and an off-source "sky" position is 2 minutes (Luhman et al. 1995). In the observations of the Magellanic Clouds, we chopped the secondary mirror from the source to $\Delta\alpha = +16'$ or $-16'$ at 0.25 Hz in the H band and 0.5 Hz in the K band. Each spectral step (at the same etalon plate separation) has one chopping cycle, consisting of four exposures: object $\rightarrow$ sky $\rightarrow$ sky $\rightarrow$ object. Each exposure had an integration time of 0.5 or 1 s.

In the frequency-switching mode, we tuned the Fabry-Perot interferometer to the line wavelength, λ_{on}, and a nearby wavelength free of line emission, λ_{off}. One observing cycle consists of four steps: $\lambda_{on} \rightarrow \lambda_{off} \rightarrow \lambda_{off} \rightarrow \lambda_{on}$. As is the case in the scanning mode, each step consists of one chopping cycle. We tried to place λ_{off} away from wings of the H_2 instrument spectral profile for λ_{on} and at positions away from telluric OH lines (see Table 2).

---

[7] The equivalent-disk size, θ_{ED}, is the diameter of a cylindrical beam whose solid angle is same as the integrated solid angle of the actual beam pattern.

TABLE 1

H$_2$ Lines and Instrument Parameters

H$_2$ Line	λ[a] (μm)	Date	θ_{ED}[b] (arcsec)	F[c]	m[d]	ΔV_{FWHM}[e] (km s^{-1})	ΔV_{BW}[f] (km s^{-1})
(5, 3) O(3)......	1.61308	1995 Oct	81.0	23.0	125	104	163
(1, 0) S(1)	2.12125	1995 Oct	81.0	25.4	94	125	196
		1994 Dec	88.9	26.4	94	120	189
(2, 1) S(1)	2.24710	1994 Dec	88.9	26.4	89	127	199

[a] Wavelength in air (Black & van Dishoeck 1987).
[b] Beam size (equivalent disk). Beam profiles are shown in Fig. 1.
[c] Effective finesse of the Fabry-Perot interferometer, including the reflectivity, parallelism, surface quality, and incident angles.
[d] Order of interference.
[e] Full-width at half-maximum of the instrument profile of an extended source.
[f] $\Delta V_{BW} = \int I(V)dV/I_{peak}$. $I(V)$ is the instrument profile of an extended source.

For flux calibration, we measured HR 1713 (B8 I, $m_K = +0.18$ mag) in 1994 December and HR 8728 (A3 V, $m_H = +1.03$ mag and $m_K = +1.00$ mag) in 1995 October. Even though the beam sizes of the 1994 December run and the 1995 October run are different, H$_2$ (1, 0) S(1) intensities measured at the same positions on both runs agree to within the errors. The absolute flux calibration is accurate to $\pm 20\%$.

2.2. CO $J = 1-0$ Emission Line

We observed the CO $J = 1 \rightarrow 0$ line in 1995 December at the SEST[8] located on La Silla in Chile. The beam size (FWHM) of the SEST is 45″. The CO intensities presented in this paper are the main beam brightness temperatures, T_{MB} (see the convention of Mangum 1993). The online temperature, T_A^*, has been converted to T_{MB} by dividing by 0.7 (which is the product of the forward spillover and scattering

TABLE 2

Frequency Switching Parameters

Object	H$_2$ Line	On μm	On km s^{-1}	Off μm	Off km s^{-1}
SMC	(5, 3) O(3)	1.61386	+124	1.61506	+347
	(1, 0) S(1)	2.12219	+112	2.12069	−100
LMC......	(5, 3) O(3)	1.61464	+274	1.61584	+477
	(1, 0) S(1)	2.12321	+261	2.12171	+49
	(2, 1) S(1)	2.24935	+249	2.24785	+49

[8] The Swedish-ESO Submillimeter Telescope, SEST, is operated jointly by ESO and the Swedish National Facility for Radio Astronomy, Onsala Space Observatory at Chalmers University of Technology.
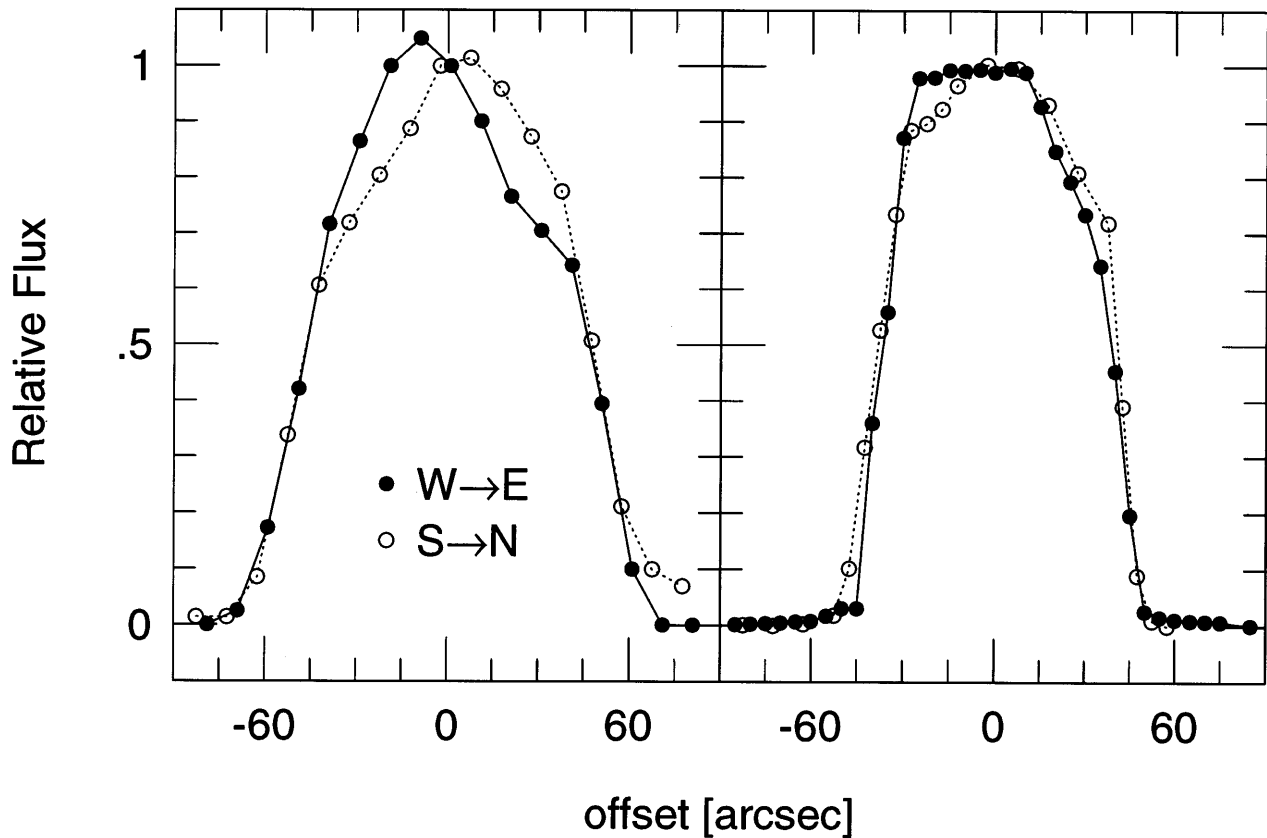

FIG. 1.—Beam profiles of the University of Texas Near-Infrared Fabry-Perot Spectrometer at the CTIO 1.5 m telescope in 1994 December (*left panel*) and 1995 October (*right panel*).
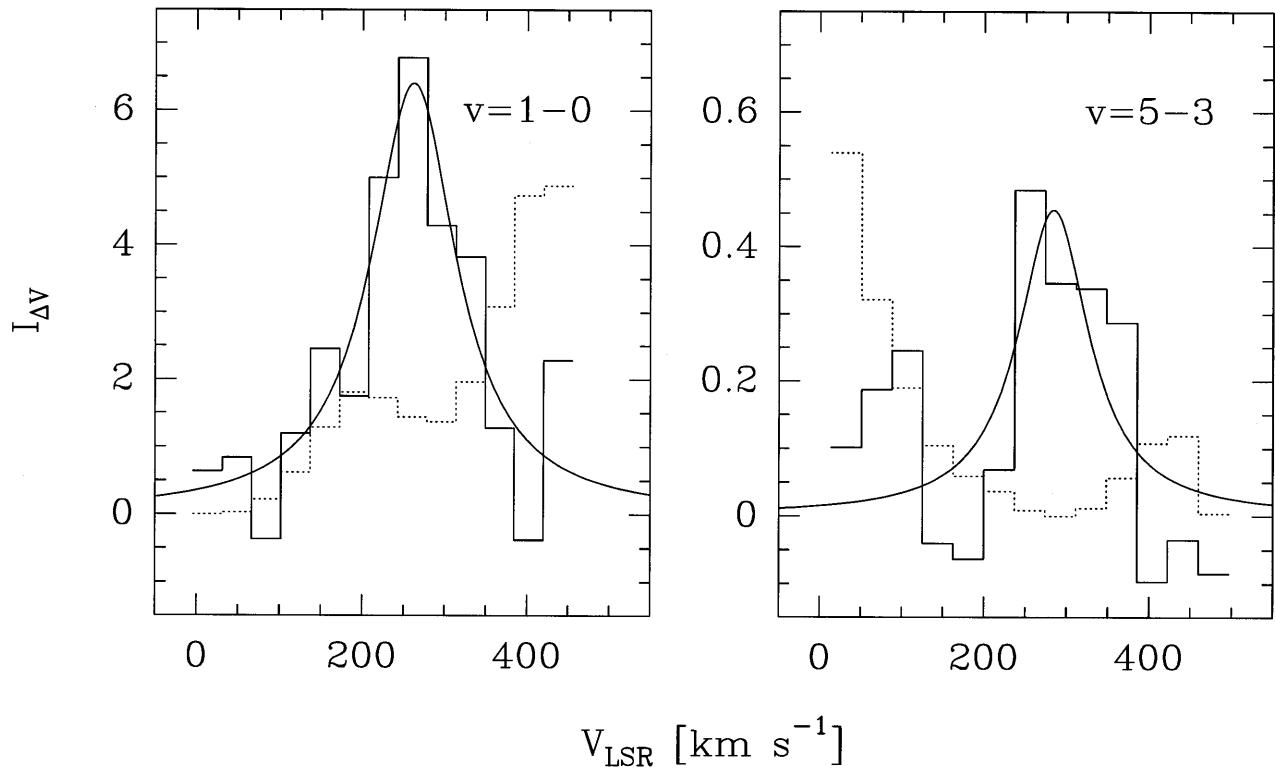
Fig. 2.—Spectra of H_2 (1, 0) $S(1)$ and (5, 3) $O(3)$ emission lines (*solid histogram*) at the (0, 0) position of 30 Doradus in units of 10^{-8} ergs s^{-1} cm^{-2} sr^{-1} (km s^{-1})$^{-1}$. The smooth curve shows a fit to the spectra with the instrument parameters using GaussFit (Jefferys 1990). The overlapped telluric OH lines (*dotted line*), measured at an off-source position, are scaled down by 20 on the H_2 (1, 0) $S(1)$ spectrum and by 100 on the H_2 (5, 3) $O(3)$ spectrum.

efficiency, and the main beam efficiency). We used frequency switching to gain a factor of 2 in observing time and to avoid possible emission from reference positions. Since this method can leave residual ripples in the spectra, the detection limit for weak signals is determined by the ripple. For some positions, we complemented the frequency-switched data with beam-switched data with a reference beam about 12′ away in azimuth. For example, in the 30 Doradus (0, −6′) region it turned out to be impossible to use the frequency-switched data.

We mapped CO $J = 1 \to 0$ spectra around positions where we detected H_2 emission and where the CO emission was below the lowest contour level (3 K km s^{-1}) of previously published CO maps (Booth 1993; Johansson et al. 1994). The CO maps are fully sampled on 20″ grids within each 81″ H_2 beam. In a single 45″ beam, the typical rms noise is 0.07 K for a channel spacing of 0.45 km s^{-1}, and the typical 1 σ statistical uncertainty of the intensity $I = \int T_{MB}\, dv$, integrated over a velocity range of 15 km s^{-1}, is 0.2 K km s^{-1}.

3. RESULTS

In low-metallicity objects, the low dust abundance allows far-UV photons to penetrate for long distances beyond the H II/H boundary. One possible scenario is that the transparency to UV photons leads to substantial regions of neutral gas, where far-UV photons have dissociated CO but where self-shielding permits hydrogen to be primarily in the form of H_2. Especially in the N159/N160 complex, the published maps show the [C II] 158 μm emission (Israel et al. 1996) extending farther than the CO $J = 1 \to 0$ emission (Johansson et al. 1994). These existing observations make such a possibility seem reasonable in the LMC.

Near-IR H_2 emission in response to far-UV radiation provides a direct test for the presence of molecular gas near cloud boundaries, albeit with no information about column density or total abundance. We selected observing targets in regions of the LMC where high spatial resolution ($\sim 1′$) [C II] maps and CO $J = 1 \to 0$ maps existed (Booth 1993; Johansson et al. 1994; Poglitsch et al. 1995; Israel et al. 1996). In the SMC, our H_2 observations cover positions for which there were CO $J = 1 \to 0$ data available (Rubio et al. 1993), but do not coincide with the observed [C II] positions (Israel & Maloney 1993). Table 3 lists the observed sources and their reference (0, 0) positions.

3.1. H_2, CO, [C II], and Far-IR

The H_2 (1, 0) $S(1)$ line intensity in the surveyed regions is $< 4 \times 10^{-6}$ ergs s^{-1} cm^{-2} sr^{-1}, except in the central

TABLE 3

OBJECT LIST

Object[a]	α_{1950}	δ_{1950}	Reference
DEM S 16	00 43 33.4	−73 39 05	1
DEM S 37	00 46 16.2	−73 32 47	1
LI-SMC 36......	00 44 50.5	−73 22 23	1
30 Dor...........	05 39 11.5	−69 06 00	2
N159/N160......	05 40 18.2	−69 47 00	3

NOTE.—Units of right ascension are hours, minutes, and seconds, and units of declination are degrees, arcminutes, and arcseconds.

[a] (0, 0) position.

REFERENCES.—(1) Based on the CO survey of the ESO-SEST Key Program (Rubio et al. 1993); (2) The CO peak (Poglitsch et al. 1995); (3) Center of the CO map in the N159/N160 region (Booth 1993; Johansson et al. 1994). Because the reference position of N160 is also the N159 (0, 0) position, the center of N160 is close to the (−1′, 7′) position in this reference system.

TABLE 4

INTENSITIES FROM THE MAGELLANIC CLOUDS

Object	$\Delta\alpha$[a] (arcmin)	$\Delta\delta$[a] (arcmin)	H_2[b] (10^{-6}) I[g]	σ[g]	CO[c] $(K\ km\ s^{-1})$ I	σ	C II[d] I[g] (10^{-4})	Far-IR[e] I[g] (10^{-2})	T_{dust}[f] (K)	Reference (CO; C II)
DEM S 16	+0.11	−0.12	3.43	0.66	2.19	0.11	...	0.43	49	2; —
	+0.11	+0.88	1.60	0.66	2.39	0.11	...	0.27	42	2; —
DEM S 37	+0.38	−3.35	0.99	2.20	...	...	...	...	...	
	−0.02	−0.05	2.4	1.1	0.584	0.073	...	0.65	45	1; —
LI-SMC 36......	−3	0	1.33	1.77	...	...	...	...	...	
	0	0	3.2	1.3	6.20	0.060	...	0.33	42	1; —
30 Dor...........	0	−1.5	4.2	2.7	2.87	...	2.6	14	45	3; 3
	−1.5	0	5.3	2.2	3.45	...	4.2	18	51	3; 3
	0	0	10.8	0.93	10.5	...	8.1	35	75	3; 3
	+1.5	0	8.6	2.4	2.23	...	3.7	7.8	44	3; 3
	0	+1.5	3.8	2.9	3.39	...	2.9	6.6	42	3; 3
	3	−9	0.94	0.75	...	3[h]	...	1.4	43	4; —
	0	−6	1.63	0.78	0.746	0.052	...	2.6	43	1; —
	−6	0	−0.28	0.53	...	3[h]	...	1.2	56	4; —
N159	−0.5	−5	2.1	1.5	25.0	0.14	...	0.31	34	5; —
	+1	−5	0.94	0.90	46.0	0.14	...	0.32	35	5; —
	−2.5	0	0.5	1.9	29.4	0.14	0.77	1.8	31	5; 6
	−1.5	0	4.5	1.4	47.3	0.14	2.3	7.1	46	5; 6
	0	0	3.23	0.99	7.70	0.052	2.5	8.2	42	1; 6
	+1	+1	4.8	1.3	19.8	0.052	2.9	8.7	56	1; 6
	0	+3	1.80	0.72	0.634	0.052	1.0	1.7	46	1; 6
N160	0	+4.5	0.8	1.2	...	3[h]	0.49	1.2	37	5; 6
	−2.5	+7	1.95	0.80	1.59	0.073	0.77	2.6	36	1; 6
	−1	+7	6.45	0.91	9.89	0.073	2.0	15	76	1; 6
	0	+7	2.46	0.71	5.82	0.073	1.7	6.5	54	1; 6
	−2	+8	1.86	0.64	4.25	0.073	1.1	2.9	39	1; 6
	0	+8	2.18	0.56	6.76	0.073	1.1	1.8	34	1; 6
	−3	+9	−0.21	0.65	...	3[h]	0.68	0.97	35	5; 6
	−1	+9	1.98	0.59	2.76	0.073	0.75	1.1	34	1; 6
	−2	+10	1.72	0.51	1.64	0.073	0.55	1.0	46	1; 6
	0	+10	2.05	0.52	3.86	0.073	0.36	0.75	43	1; 6
	−1	+12	−0.6	1.3	4.49	...	...	0.71	41	5; —

[a] Offset from the object (0, 0) position.
[b] Measured H_2 (1, 0) $S(1)$ intensity with 1 σ uncertainty.
[c] Velocity-integrated CO $J = 1 \rightarrow 0$ intensity, $I = \int T_{MB}\,dv$. 1 K km s^{-1} = 1.57×10^{-9} ergs s^{-1} cm^{-2} sr^{-1}.
[d] [C II] 158 μm intensity.
[e] IRAS far-IR continuum intensity. See equation (1).
[f] Dust temperature deduced from the ratio $I_{60\ \mu m}/I_{100\ \mu m}$. See equation (2).
[g] In units of ergs s^{-1} cm^{-2} sr^{-1}.
[h] Upper limit that lies beyond the lowest contour ($\int T_{MB}\,dv = 3$ K km s^{-1}) in the published CO maps (Booth 1993; Johansson et al. 1994). See also Figs. 3 and 4.
REFERENCES.—(1) This work; (2) Rubio et al. 1993; (3) Poglitsch et al. 1995; (4) Booth 1993; (5) Johansson et al 1994; (6) Israel et al. 1996.

regions of 30 Doradus and N160. About 70% of the observed points have detections of the (1, 0) $S(1)$ line with a significance of 2 σ or more. The H_2 (1, 0) $S(1)$ intensities are listed in Table 4, and the H_2 (2, 1) $S(1)$ and (5, 3) $O(3)$ intensities are listed in Table 5. Reddening toward the stars in the LMC has been measured using $(U-B)$ and $(B-V)$ colors. The Galactic foreground extinction, A_V, toward the LMC is 0.23 ± 0.07 mag (Greve, van Genderen, & Laval 1990; Lee 1991). Applying $A_K = 0.112\ A_V$ (Rieke & Lebofsky 1985), the foreground A_V implies a negligible A_K of ~ 0.03 mag. The molecular clouds in the LMC may, however, extinguish the H_2 emission from their own back

TABLE 5

H_2 LINE RATIOS

OBJECT	$\Delta\alpha$ (arcmin)	$\Delta\delta$ (arcmin)	(2, 1) $S(1)$ Intensity[a] (10^{-6})	Ratio[b]	(5, 3) $O(3)$ Intensity[a] (10^{-6})	Ratio[b]
DEM S 16......	+0.11	−0.12	...	...	0.76 ± 0.34	0.22 ± 0.11
	+0.11	+0.88	...	...	0.27 ± 0.36	0.17 ± 0.24
30 Dor	0	0	4.0 ± 1.5	0.37 ± 0.14	1.48 ± 0.37	0.138 ± 0.036
	+1.5	0	...	...	1.42 ± 0.51	0.166 ± 0.075
N159	+1	+1	...	...	0.65 ± 0.41	0.135 ± 0.091
N160	−1	+7	3.6 ± 1.9	0.56 ± 0.30	2.36 ± 0.41	0.366 ± 0.082

[a] Measured intensity with 1 σ statistical uncertainty in units of ergs s^{-1} cm^{-2} sr^{-1}.
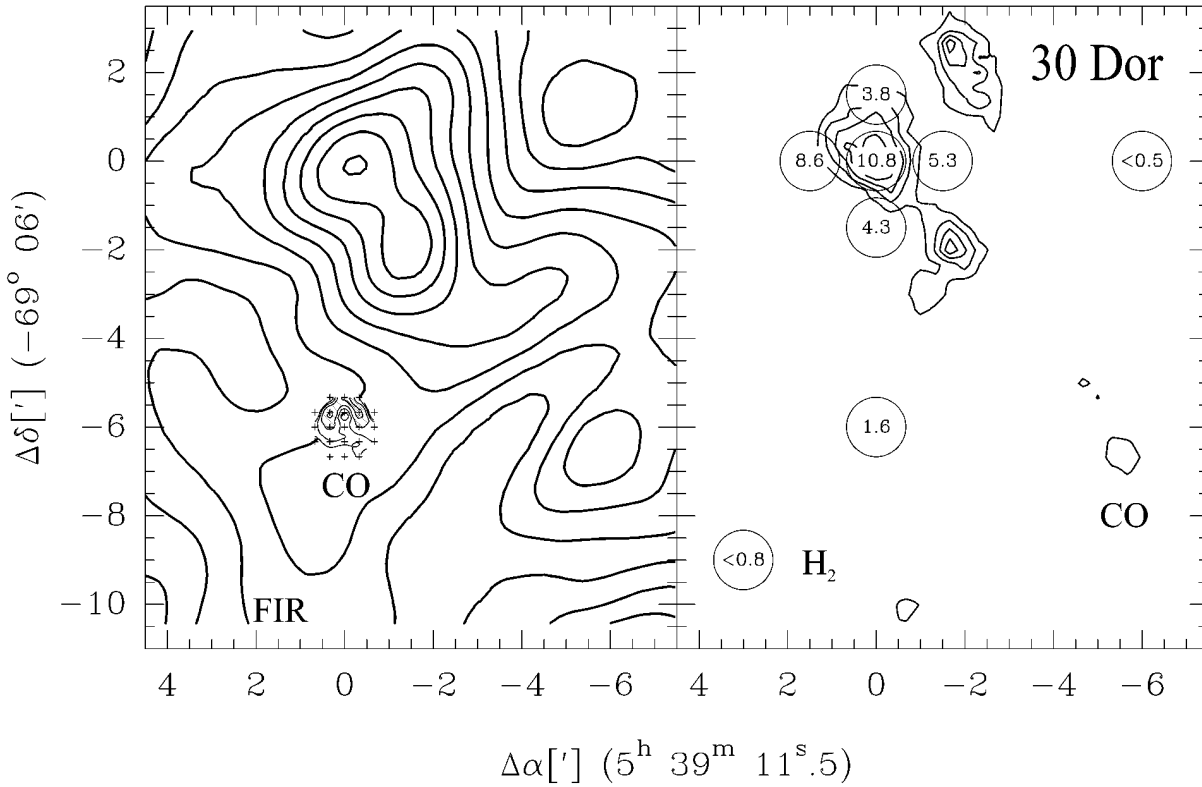[b] Intensity ratio with respect to the (1, 0) $S(1)$ line intensity.

FIG. 3.—Intensity maps of the 30 Doradus region. The (0, 0) position is $\alpha_{1950} = 5^h39^m11^s5$ and $\delta_{1950} = -69°6'0''$. The axes show the R.A. and decl. offset in arcminutes. *Left panel*: *IRAS* far-IR continuum map (*thick lines*) and new CO $J = 1 \to 0$ map (*thin lines near* [0, $-6'$]). The far-IR intensities are calculated from the observed $I_{60\,\mu m}$ and $I_{100\,\mu m}$ using eq. (1). The CO intensity data are obtained from this work, and the crosses show the observed positions. The contours are spaced at logarithmic intervals: $I_{FIR} = 0.398, 0.631, 1.00, 1.58, 2.51, 3.98, 6.31, 10.0, 15.8, 25.1, 39.8$ (i.e., $10^{0.2n}$, $n = -2, -1, \ldots, 8$) in units of 10^{-2} ergs s^{-1} cm^{-2} sr^{-1}, and $\int T_{MB}\,dv = 0.398, 0.631, 1.00, 1.58$ (i.e., $10^{0.2n}$, $n = -2, -1, 0, 1$) in units of K km s^{-1}. *Right panel*: Plotted H$_2$ (1, 0) S(1) data (within the circles) overlaid onto the published CO $J = 1 \to 0$ map. Numbers are in units of 10^{-6} ergs s^{-1} cm^{-2} sr^{-1}, and the size of the circles are the equivalent-disk size of the UT FPS beam. For the CO data (Booth 1993; Johansson et al. 1994), the contours are spaced linearly: $\int T_{MB}\,dv = 3, 6, 9, \ldots$ in units of K km s^{-1}.

sides. Section 5.3 discusses the H$_2$ emission from the back side of the clouds.

Table 4 lists the CO $J = 1 \to 0$ and [C II] intensities convolved to the beam size of the H$_2$ observations ($\theta_{ED} = 81''$). We assumed that the beam profile of the University of Texas Fabry-Perot Spectrometer is a box function.

The columns for far-IR intensity and dust temperature in Table 4 are from the *IRAS* data processed at IPAC[9] using standard HIRES processing. The HIRES processor enhances the spatial resolution of *IRAS* images using a maximum correlation method algorithm (Aumann, Fowler, & Melnyk 1990). The effective resolutions are 1$'$.0–1$'$.6 at 60 μm and 1$'$.6–2$'$.4 at 100 μm. We calculate the integrated far-IR intensity using the approximation of Helou et al. (1988):

$$I_{FIR} = 1.26 \times 10^{-5}(2.58 I_{60\,\mu m} + I_{100\,\mu m}) , \qquad (1)$$

where $I_{60\,\mu m}$ and $I_{100\,\mu m}$ are in units of MJy sr^{-1} and I_{FIR} is in ergs s^{-1} cm^{-2} sr^{-1}. This equation is valid within 20% errors when 31 K $< T_{dust} <$ 58 K. We deduce the dust temperature, T_{dust}, from the ratio of 60 μm to 100 μm intensity:

$$\frac{I_{60\,\mu m}}{I_{100\,\mu m}} = \left(\frac{\nu_{60\,\mu m}}{\nu_{100\,\mu m}}\right)^4 \frac{\exp{(h\nu_{100\,\mu m}/kT_{dust})} - 1}{\exp{(h\nu_{60\,\mu m}/kT_{dust})} - 1} , \qquad (2)$$

where h is Planck's constant, k is Boltzmann's constant, and ν is the frequency in units of Hz. In the above equation, we

assume that the 60 μm emission is not dominated by small ($D \simeq 5$ nm), thermally spiking grains but by large grains in steady-state temperatures (Draine & Lee 1984), and that the dust emissivity (Q_ν) is proportional to ν^n where the dust emissivity index, n, is 1.

3.2. H$_2$ Results

3.2.1. Small Magellanic Cloud

In the SMC, we detected H$_2$ (1, 0) S(1) emission, with S/N > 2, near *IRAS* sources in the DEM S 16, DEM S 37, and LI-SMC 36 regions. Toward supernova remnants, e.g., DEM S 37 ($+0'.38$, $-3'.35$) and LI-SMC 36 ($-3'$, 0), we did not detect H$_2$ emission at a 1 σ level of $\sim 2 \times 10^{-6}$ ergs s^{-1} cm^{-2} sr^{-1}.

3.2.2. Large Magellanic Cloud: 30 Doradus

Figure 3 shows the far-IR, CO $J = 1 \to 0$, and H$_2$ (1, 0) S(1) intensity maps of the 30 Doradus region. At the 30 Doradus (0, 0) point, the intensity of the H$_2$ (1, 0) S(1) line, I_{H_2}, is 1.1×10^{-5} ergs s^{-1} cm^{-2} sr^{-1} in our 81$''$ beam [hereafter I_{H_2} denotes the intensity of the H$_2$ (1, 0) S(1) line]. Poglitsch et al. (1995), using their imaging NIR spectrometer FAST, observed intense H$_2$ (1, 0) S(1) emission around the central cluster R136 and showed that the H$_2$ source appears highly fragmented ($<5''$ or 1 pc scale), with a typical intensity of $\sim 1.6 \times 10^{-4}$ ergs s^{-1} cm^{-2} sr^{-1}.

Our observations show that the H$_2$ emission in 30 Doradus is very extended, >40 pc, compared to the known extent of the CO $J = 1 \to 0$ emission (~ 35 pc, see the right
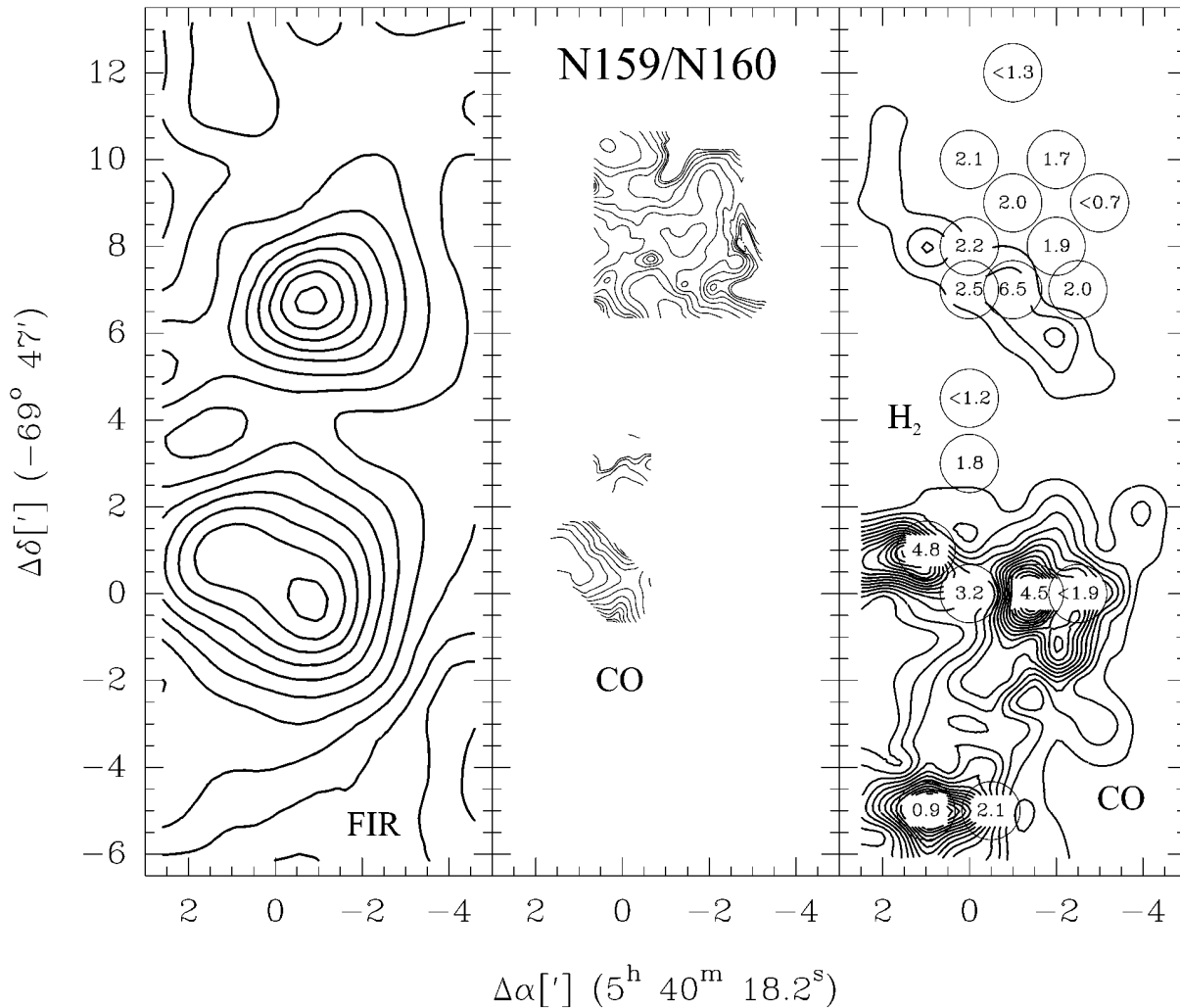
Fig. 4.—Intensity maps of the N159/N160 region. *Left panel*: Far-IR continuum map. Contour intervals are spaced at logarithmic intervals: $I_{FIR} = 0.158$, 0.251, 0.398, 0.631, 1.00, 1.58, 2.51, 3.98, 6.31, 10.0, 15.8 in units of 10^{-2} ergs s^{-1} cm^{-2} sr^{-1}. The far-IR peak at $(-1', +7')$ is near N160 and the peak at $(-1', 0)$ is near N159. *Middle panel*: New CO $J = 1 \to 0$ map. See caption for Fig. 5, which shows the same data. *Right panel*: Plotted H$_2$ (1, 0) S(1) data (within the circles) overlaid on the published CO $J = 1 \to 0$ map. See caption for right map of Fig. 3.

map in Fig. 3). At $1\overset{.}{'}5$ (or 22 pc) from the (0, 0) position, the H$_2$ (1, 0) S(1) intensity is only a factor of 2 lower than at the peak (see Fig. 3). We also detected faint H$_2$ (1, 0) S(1) emission at (0, $-6'$), $I_{H_2} = 1.6 \times 10^{-6}$ ergs s^{-1} cm^{-2} sr^{-1}, where CO $J = 1 \to 0$ emission had not been detected during the survey of the ESO-SEST Key program (Booth 1993).

3.2.3. *Large Magellanic Cloud: N159/N160*

The N159/N160 H II complexes are 40′ south of 30 Doradus. The [C II] line (Israel et al. 1996) and the far-IR continuum distributions (left map in Fig. 4) show that the far-UV fields are strong near both N159 and N160. On the other hand, the CO intensity around N159 is more than 4 times stronger than that around N160.

The H$_2$ (1, 0) S(1) line has been detected at N159 Blob (a compact H II source with a size of $8'' \times 6''$; Heydari-Malayeri & Testor 1985) by several groups. In Table 6, we compare the previous data with our new results. The flux increases as the beam size increases. This suggests that if there is a single source, the emission region is more extended than $\sim 20''$. Alternatively, there could be clumpy emission filling our $81''$ beam with an area covering factor of $\sim 20\%$ of the covering factor in the inner $6'' \times 6''$ region. In our H$_2$ survey, we observed very extended ($>5'$ or 70 pc)

H$_2$ (1, 0) S(1) emission from the N159/N160 H II complex (see the right map in Fig. 4). In the N159 region, we detected H$_2$ emission where the CO cloud complex is bright and extended (see Fig. 1 in Johansson et al. 1994). In the N160 region, however, we also detected H$_2$ emission beyond the lowest CO $J = 1 \to 0$ contour level (3 K km s^{-1}) in the map of Johansson et al. (1994).[10] In spite of the weak or absent CO emission in the N160 region, the H$_2$ observations indicate that the size of the molecular cloud complex is as big as that in the N159 region.

3.3. CO $J = 1 \to 0$

At several positions in the outer regions of 30 Doradus and N160, we detected H$_2$ emission where earlier CO surveys failed to detect the $J = 1 \to 0$ line. In order to determine whether all CO is dissociated at these positions, we observed the regions again in the CO $J = 1 \to 0$ line (see § 2.2) with higher sensitivity ($\sigma \simeq 0.2$ K km s^{-1}) than the

---

[10] See also Figure 2 of Israel et al. (1996), which used the data of Johansson et al. (1994). More recently, the SEST Key program has observed more positions in 30 Doradus and N159/N160 (Johansson et al. 1998).

TABLE 6

COMPARISON WITH OTHER H_2 (1, 0) S(1) DATA IN N159

Reference	Position[a] (arcmin)	Beam Size[b] (arcsec)	Ω[c] (10^{-9} sr)	Flux[d] (10^{-14})	Intensity[e] (10^{-6})
1	+1.11, +0.85	6 × 6	0.85	1.7	20
2	+1.11, +0.85	ϕ13	3.1	5.2	17
3	+1.11, +0.85	10 × 21	5.0	8.5	17
4	+1.0, +1.0	ϕ81	121	58	4.8

[a] Offset from the N159 (0, 0) position (see Table 3). +1.11, +0.85 corresponds to the N159 Blob (Heydari-Malayeri & Testor 1985).

[b] ϕ13 denotes $\theta_{ED} = 13''$.

[c] Solid angle of the beam.

[d] In units of ergs s^{-1} cm^{-2}.

[e] In units of ergs s^{-1} cm^{-2} sr^{-1}.

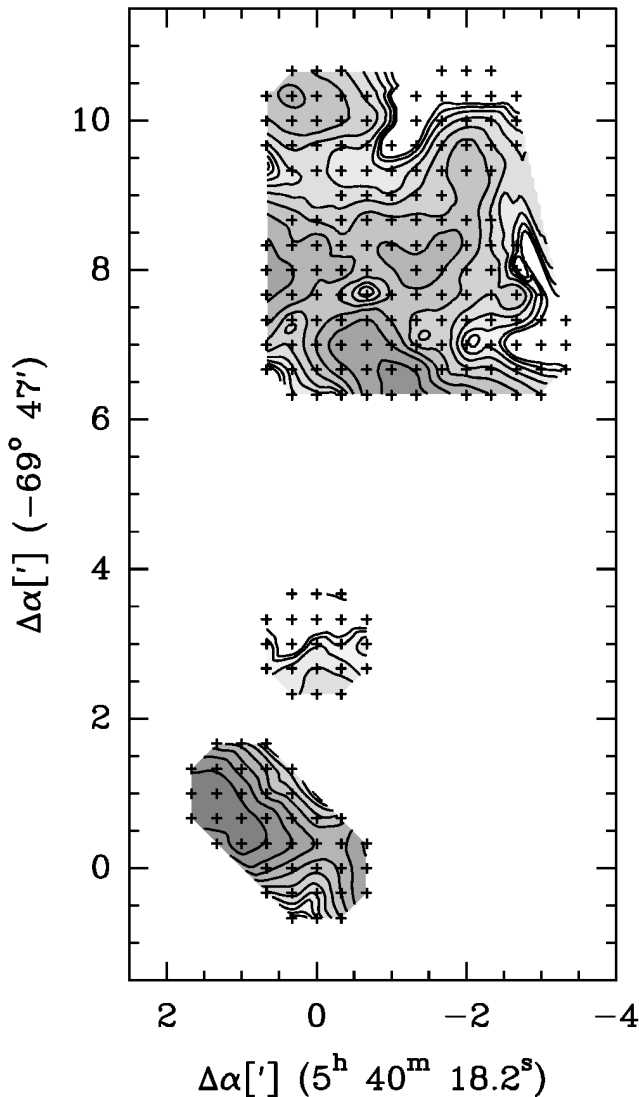REFERENCES.—(1) Israel & Koornneef 1992; (2) Krabbe et al. 1991; (3) Kawara et al. 1988; (4) This paper.

FIG. 5.—New CO $J = 1 \rightarrow 0$ intensity map of the N159/N160 region. The contours are spaced at logarithmic intervals: for the $(-1', +8\!.\!5)$ region, $\int T_{MB} dv = 0.398, 0.631, 1.00, 1.58, 2.51, 3.98, 6.31, 10.0, 15.8$ K km s^{-1}; for the (0, +3′) region, 0.398, 0.631, 1.00, 1.58 K km s^{-1}; for the $(+0\!.\!5, +0\!.\!5)$ region, 0.398, 0.631, 1.00, 1.58, 2.51, 3.98, 6.31, 10.0, 15.8, 25.1 K km s^{-1}. Observed positions are plotted in plus signs.

previous observations, of which the lowest contour level was 3 K km s^{-1} (Booth 1993; Johansson et al. 1994).

We made a fully sampled CO map inside the UT FPS beam at (0, −6′) in 30 Doradus, and detected CO $J = 1 \rightarrow 0$ at a level of 0.5 K km s^{-1} (see Fig. 3). We also made CO maps in the outer regions of N160, where the previous CO $J = 1 \rightarrow 0$ map did not show any CO emission, and sampled some positions in N159 to confirm the flux calibration of the new observations (see Figs. 4 and 5). We plot the contours at logarithmic intervals to emphasize the edges of the molecular cloud complexes; note the dense contour lines at the northwestern and western sides of the N160 complex. The CO $J = 1 \rightarrow 0$ emission regions cover the H_2 emission regions except at the $(-2\!.\!5, +7')$ and the $(-2', +10')$ positions, where the CO cloud complex fills 50%–70% of the H_2 beams.

3.4. H_2 Excitation Mechanism

Table 5 lists the observed H_2 (2, 1) S(1)/(1, 0) S(1) and (5, 3) O(3)/(1, 0) S(1) line ratios in the Magellanic Clouds. Observations of the H_2 lines in archetypal shocked regions, e.g., Orion BN-KL, HH 7, and the supernova remnant IC 443, show that the H_2 ratios of (2, 1) S(1)/(1, 0) S(1) are almost constant at ~ 0.08, or $T_{exc} \simeq 2 \times 10^3$ K (Burton et al. 1989; Richter, Graham, & Wright 1995). Assuming that the excited levels are in LTE and $T_{exc} = 2000$ K, the (5, 3) O(3)/(1, 0) S(1) ratio should be only $\sim 9 \times 10^{-5}$.

Molecular hydrogen in PDRs absorbs 91.2–110.8 nm photons in the $B^1\Sigma_u^+ - X^1\Sigma_g^+$ Lyman and $C^1\Pi_u - X^1\Sigma_g^+$ Werner bands. About 15% of the electronically excited molecules are dissociated (Draine & Bertoldi 1996). The remaining 85% of the excitations result in populations of various ro-vibration levels of the ground electronic state. If $n(H_2) < 5 \times 10^4$ cm^{-3}, the relative line intensities arising in UV-excited H_2 are insensitive to density or to UV field strength (Black & van Dishoeck 1987). In this pure fluorescent transition case, the H_2 ratio of (2, 1) S(1)/(1, 0) S(1) is 0.56 and that of (5, 3) O(3)/(1, 0) S(1) is 0.38. At densities of $\geq 5 \times 10^4$ cm^{-3} (Luhman et al. 1997), the collisional deexcitation of UV-pumped H_2 begins to affect the ro-vibrational level populations. If the PDR boundaries become sufficiently warm ($T > 1000$ K) and dense ($\geq 5 \times 10^4$ cm^{-3}), collisional excitation thermalizes the low vibrational ($v \leq 2$)

level populations (Sternberg & Dalgarno 1989; Luhman et al. 1997).

Detections of the H_2 (5, 3) $O(3)$ line in the Magellanic Clouds (Table 5) verify the UV-excitation of H_2. The observed H_2 line ratios from the N160 region are those expected for pure fluorescence. The ratios toward other regions show that the H_2 ro-vibration levels may be affected somewhat by collisions. In 30 Doradus, the peak H_2 (1, 0) $S(1)$ intensity is 2.3×10^{-4} ergs s^{-1} cm^{-2} sr^{-1} (Poglitsch et al. 1995), which is brighter than the maximum predicted by our PDR models ($I_{H_2} \leq 9.6 \times 10^{-5}$ ergs s^{-1} cm^{-2} sr^{-1}; see Fig. 12). The models may underestimate the intensity by as much as a factor of 2 in regions with high densities and high UV fields by neglecting the large increase in UV pumping in the very warm (420–600 K) region at the cloud edge. Alternatively, there may be some collisional excitation of H_2 $v = 1$ as well as collisional deexcitation of the high-v states, as one finds in clouds subjected to intense far-UV fields (Luhman et al. 1997).

4. COMPARING WITH GALACTIC CLOUDS

We compare the H_2 (1, 0) $S(1)$, [C II] 158 μm, CO $J = 1 \rightarrow 0$, and far-IR emission from the clouds in the Magellanic Clouds (see Table 4) to the emission from star-forming clouds in Orion and NGC 2024 for which we have comparable data sets (see Table 7). In the LMC, we select positions where complete H_2, [C II], and CO data sets exist: five positions in the 30 Doradus region, four positions in the N159 region, and eight positions in the N160 region. In the SMC, we use four positions with only CO and H_2 data.

4.1. Data from NGC 2024 and Orion A Star Formation Regions

For the Galactic cloud data, we make use of the published H_2 (1, 0) $S(1)$, [C II] 158 μm, and CO $J = 1 \rightarrow 0$ data in Schloerb & Loren (1982), Stacey et al. (1993), Jaffe et al. (1994), Luhman et al. (1994), Luhman & Jaffe (1996), and Luhman et al. (1997). The far-IR data are from the HIRES-

processed *IRAS* data (see § 3.1). In the Orion molecular cloud, Stacey et al. (1993) made two [C II] strip maps in right ascension, both of which pass close to the CO $J = 1 \rightarrow 0$ peak. The [C II] flux along the strips was bootstrapped—integrated by assuming zero flux at the ends of the cut and summing the chopped differences. The data from cut 1 (observed west to east) and cut 2 (observed east to west) are not in complete agreement; therefore, we take only those data with

$$2 \frac{|I_{\text{cut 1}} - I_{\text{cut 2}}|}{I_{\text{cut 1}} + I_{\text{cut 2}}} < 0.4 . \tag{3}$$

We also exclude positions at which the *IRAS* data are saturated, i.e., $I_{60 \, \mu m} > 1500$ MJy sr^{-1}, and where the H_2 ro-vibrational level populations begin to show effects of collisional deexcitation [(6, 4) $Q(1)/(1, 0)$ $S(1) < 0.15$; see Table 2 of Luhman & Jaffe 1996]. Some positions where collisional deexcitation was unlikely were not observed in the H_2 (6, 4) $Q(1)$ line but are included in the data we use (see discussion in § 5.5.1). Table 7 lists the compiled data sets in the Galactic clouds: four positions from the Orion A molecular cloud (hereafter Orion), and 11 positions from the cloud associated with the NGC 2024 H II region (hereafter NGC 2024).

Figure 6 compares the data from 15 positions in the Galactic clouds with the data of Jaffe et al. (1994), who presented CO $J = 1 \rightarrow 0$ and [C II] data from NGC 2024 and showed that the different parts of the source have very different distributions on a $I_{C II}$ versus I_{CO} plot. The left panel in Figure 6 shows the distinction between the *cloud proper zone* ($\Delta\alpha > -10'$ with respect to NGC 2024 IRS 1; *open circles*) and the *western edge zone* ($\Delta\alpha < -10'$; *open triangles*) in NGC 2024. Data from the cloud proper zone agree with the PDR models of Wolfire, Hollenbach, & Tielens (1989), while many of the $I_{C II}/I_{CO}$ ratios toward the western edge zone are much higher than any of the model ratios. Jaffe et al. (1994) interpreted the western edge zone results as implying that the mean column density of clouds

TABLE 7
INTENSITIES FROM THE GALACTIC CLOUDS

OBJECT[a]	$\Delta\alpha$ (arcmin)	$\Delta\delta$ (arcmin)	H_2 (10^{-6}) I[c]	σ[c]	CO I (K km s^{-1})	C II I[c] (10^{-4})	FAR-IR I[c] (10^{-2})	T_{dust} (K)	REFERENCE[b] (CO; C II)
Orion	+8	0	23	6	34.0	9.9	56	55	1; 2
	+10	0	28	5	29.0	6.1	20	39	1; 2
	+12	0	5.2	1.6	29.5	4.3	8.3	36	1; 2
	+1.84	+9.83	27	4	60.7	4.5	41	42	1; 3
NGC 2024: Edge......	−17	0	9	1.9	13.4	5.6	3.3	36	4; 4
	−16	0	12	3	18.6	6.7	4.7	37	4; 4
	−15	0	13	2	14.4	8.6	4.9	37	4; 4
	−14	0	3.3	1.2	6.70	5.0	4.3	37	4; 4
	−13	0	4.5	1.8	15.6	4.7	4.4	35	4; 4
	−12	0	6.4	1.9	51.0	5.6	6.6	38	4; 4
	−11	0	8	2	84.6	6.3	10	41	4; 4
NGC 2024: Prop......	−9	0	9	3	110	8.8	19	49	4; 4
	−8	0	6	3	132	11	15	43	4; 4
	−6	0	8	3	154	10	26	47	4; 4
	−5	0	11	4	130	9.9	55	52	4; 4

NOTE.—See footnotes to Table 4 for other columns.

[a] Orion (0, 0): $\alpha_{1950} = 5^h32^m49^s0$, $\delta_{1950} = -05°25'16''$ (θ^1 Ori C). NGC 2024 (0, 0): $\alpha_{1950} = 5^h39^m14^s0$, $\delta_{1950} = -01°57'00''$. NGC 2024: Edge and NGC 2024: Prop have the same (0, 0) position. See text for differences between NGC 2024: Edge and NGC 2024: Prop.

[b] H_2 data is from Luhman & Jaffe (1996).

[c] In units of ergs s^{-1} cm^{-2} sr^{-1}.

REFERENCES.—(1) Schloerb & Loren 1982; (2) Stacey et al. 1993; (3) Luhman et al. 1997; (4) Jaffe et al. 1994.
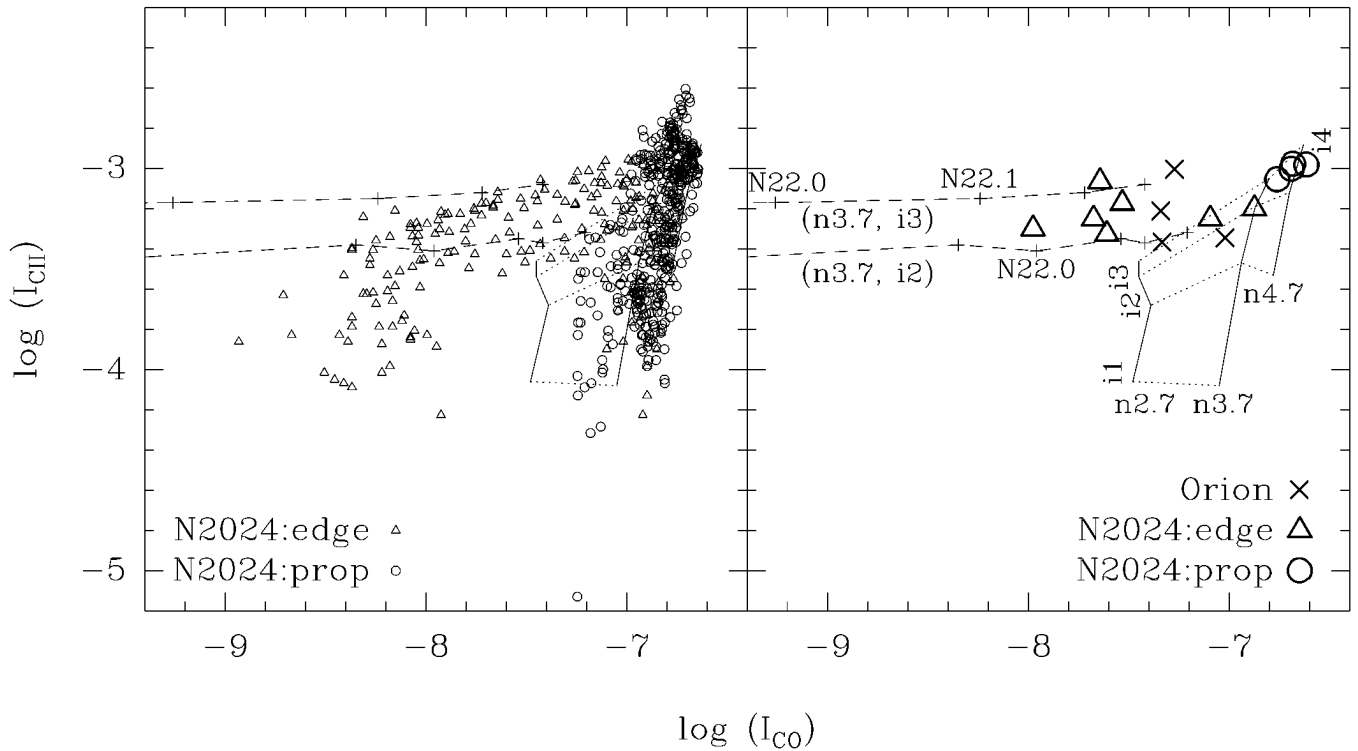
FIG. 6.—[C II] 158 μm intensity versus CO $J = 1 \rightarrow 0$ intensity in units of ergs s^{-1} cm^{-2} sr^{-1}. The left plot is replicated from Fig. 4 in Jaffe et al. (1994). The right plot shows the distribution of the Galactic data that we use in this work. We also overlay the results from the plane-parallel models, using the Galactic parameters. See Figs. 8 and 9 for explanations.

decreases to the west. The right panel in Figure 6 shows the location in the $I_{C II}$–I_{CO} space of the data sets in Table 7, which will be used to compare with those from the Magellanic Clouds.

4.2. Far-IR Data

4.2.1. I_{UV} versus I_{FIR}

The intensity of the interstellar far-UV radiation field is usually expressed in terms of the scaling factor I_{UV}, the mean intensity in the solar neighborhood (Draine 1978; also see footnote 2 in Black & van Dishoeck 1987). The critical part of the UV range for H$_2$ fluorescence, C ionization, and CO dissociation is 91.2 nm $< \lambda <$ 113 nm (Black & van Dishoeck 1987; van Dishoeck & Black 1988a). The intensity of the $I_{UV} = 1$ field integrated over 91.2 nm $< \lambda <$ 113 nm is 3.71×10^{-5} ergs s^{-1} cm^{-2} sr^{-1}. Note that some authors (e.g., Tielens & Hollenbach 1985) use Habing's (1968) determination of the local far-UV field, 1.3×10^{-4} ergs s^{-1} cm^{-2} sr^{-1}, for the integrated intensity between 6 eV $< h\nu <$ 13.6 eV or 91.2 nm $< \lambda <$ 206.6 nm, and use the symbol G_0 to indicate the degree of enhancement over this standard integrated intensity. The corresponding intensity of the Draine field integrated over the same band as used for G_0 is 2.13×10^{-4} ergs s^{-1} cm^{-2} sr^{-1} (for a detailed comparison between the Draine field and the Habing field, see Draine & Bertoldi 1996).

Most of the far-UV energy is absorbed by grains and reradiated in the far-IR:

$$I_{FIR} = 2 \times (2.13 \times 10^{-4}) I_{UV} \text{ ergs s}^{-1} \text{ cm}^{-2} \text{ sr}^{-1} , \quad (4)$$

where the factor of 2 accounts for incident radiation at longer wavelengths, $I_\nu(\lambda > 206.6 \text{ nm})$ (Wolfire et al. 1989).

4.2.2. I_{FIR} versus T_{dust}

We can use the far-IR emission to normalize the various line intensities to compensate for beam-filling factor effects. Before we do so, however, we need to understand how the far-IR emission arises. Figure 7 shows I_{FIR} versus T_{dust} for the Galactic star-forming cloud positions and the Magellanic Cloud positions in our sample. We derive I_{FIR} from the measured 60 μm and 100 μm intensities using equation (1), and derive T_{dust} using equation (2). Assuming that the dust is heated by an external far-UV field, we can approximate the results of PDR models by

$$T_{dust} = 13.5 \left(I_{UV} \frac{T_{eff}}{3 \times 10^4} \right)^{1/5} \text{ K} , \quad (5)$$

where T_{eff} is the equivalent stellar surface temperature that would produce the incident UV field (Hollenbach, Takahashi, & Tielens 1991; Spaans et al. 1994). Assuming $T_{eff} = 3 \times 10^4$ K, the expected relation between T_{dust} and I_{FIR} is

$$\log I_{FIR} = -9.02 + 5 \log T_{dust} , \quad (6)$$

which is shown as a dotted line in Figure 7.

The observed T_{dust} and I_{FIR} distributions in Orion and NGC 2024 agree with the model in equation (6). I_{FIR} is proportional to the beam-filling factor, while T_{dust}, which was deduced from the ratio of $I_{60 \mu m}/I_{100 \mu m}$, is independent of the beam-filling factor. With a beam size of $\sim 1'$ (or ~ 0.12 pc at the distance of Orion, 415 pc; Anthony-Twarog 1982), the projected beam-filling factor for the clouds in Orion and NGC 2024 is ~ 1, which explains the agreement between the observed T_{dust}-I_{FIR} relation and the model. If we assume that the dust size distribution is independent of metallicity and that the clouds are optically thick in the far-UV, the T_{dust}-I_{FIR} relation should be independent of the
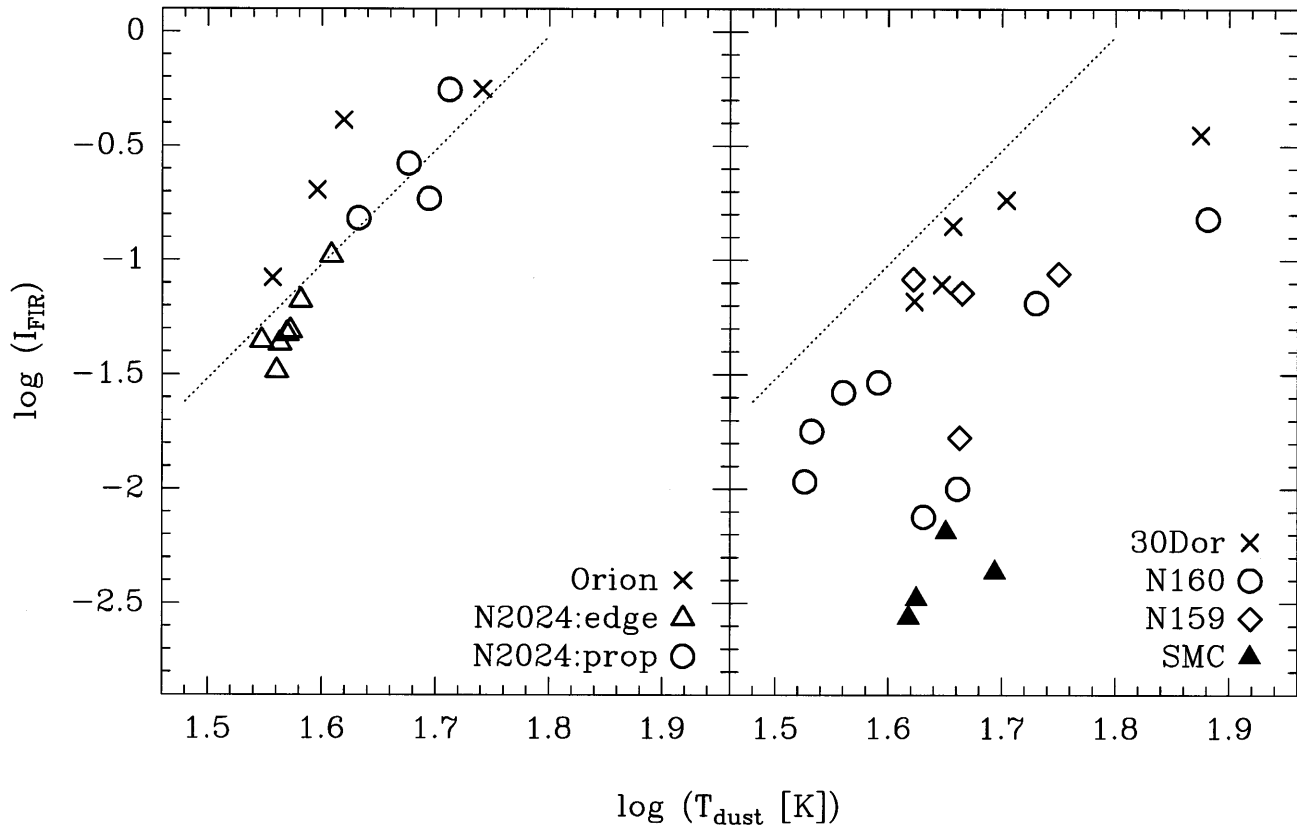
FIG. 7.—Far-IR intensities (eq. [1] and Tables 4 and 7) versus T_{dust} (eq. [2] and Tables 4 and 7). I_{FIR} is in units of ergs s^{-1} cm^{-2} sr^{-1}. Data in the left plot are from the Galactic clouds, and data in the right plot are from the LMC. Dotted line shows the model in eq. (6). We do not include the effects of spherical geometry (ϵ_{FIR}, see § 5.4) in the model calculation.

dust abundance (see § 5.2 for more discussion). For the Magellanic Clouds, the observed I_{FIR} values are an order of magnitude weaker than the values predicted by the T_{dust}-I_{FIR} relation. This difference implies a beam-filling factor in the Magellanic Clouds of ~ 0.1 ($d^{LMC} = 50.1$ kpc; Westerlund 1990).

4.3. Line Intensities Divided by I_{FIR}

The line and continuum emission we describe here arises in the layers of molecular clouds where UV photons influence the chemistry and the physical conditions. Various parameters affect the emergent intensity:

$$I_i = \eta \epsilon_i f_i(n_H, I_{UV}, \delta v_D, Z) ,$$

$$I_{FIR} = \eta \epsilon_{FIR} 2 \times 4.26 \times 10^{-4} I_{UV} , \quad (7)$$

where I_i is the observed CO $J = 1 \rightarrow 0$, [C II] 158 μm, or H$_2$ (1, 0) S(1) emission line intensity, I_{FIR} is the observed far-IR continuum intensity in units of ergs s^{-1} cm^{-2} sr^{-1}, and f_i is the combined intensity arising from the front and back sides of a plane-parallel model cloud that fills the beam. The front and back surfaces of the cloud are exposed to external far-UV radiation, and are perpendicular to the line of sight. The value of f_i depends on the hydrogen number density, $n_H = n(H) + 2n(H_2)$ [where $n(H)$ and $n(H_2)$ are the atomic and molecular hydrogen density, respectively], the far-UV field strength, I_{UV}, the Doppler velocity dispersion, δv_D (or half-width at $1/e$ point), and the metal abundance, Z. The term η is a beam-filling factor and ϵ is a geometric correction factor, which we describe below.

Unlike the substructure of the fully molecular interior of clouds, which may have many size scales, the penetration

scale length of far-UV photons and UV photochemistry insure that structures within giant molecular cloud (GMC) complexes with UV-illuminated surfaces and CO-bearing cores have a minimum size determined by their density and metallicity. Measurements and theoretical arguments show that PDR structures outside the dense cores of molecular clouds are clumpy on a size scale of ~ 1 pc (Burton, Hollenbach, & Tielens 1990; Jaffe et al. 1994), comparable to or larger than the Orion beam but very much smaller than the beams in the LMC. Since the measured intensity is a beam average over any source structure, we have to correct for the effects of different beam-filling factors in order to directly compare the emitted intensities from the LMC with those from the Galactic clouds. We define the beam-filling factor, η, as the fraction of the observed beam area filled by a single cloud (not an ensemble of clouds), using the outermost edge as the cloud boundary (or the boundary between H II and H I regions):

$$\eta = \left(\frac{2R_{cloud}}{d\theta_{ED}} \right)^2 , \quad (8)$$

where R_{cloud} is the radius of the cloud to the outer (H II/H) boundary, d is the distance to the cloud, and θ_{ED} is the diameter of the telescope equivalent disk in radians. The value of η is the same for all types of emission in the same cloud. In order to simplify model simulations in § 5, we assume that only one cloud is in the telescope beam, that the telescope has a box function beam profile, and that the telescope beam area is always larger than the cloud size, i.e., $d\theta_{ED} \geq 2R_{cloud}$, or $\eta \leq 1$.

TABLE 8

INTENSITY RATIOS BETWEEN H$_2$ (1,0) S(1), [C II], AND CO $J = 1 \rightarrow 0$

OBJECT	N[a]	log ($I_{H_2}/I_{C II}$)		log ($I_{C II}/I_{CO}$)		log (I_{H_2}/I_{CO})	
		Average[b]	s.d.[c]	Average	s.d.	Average	s. d.
Galaxy....................	15	−1.85	0.28	4.04	0.37	2.19	0.47
Orion	4	−1.53	0.31	4.01	0.25	2.48	0.32
NGC 2024:Prop......	4	−2.08	0.13	3.68	0.03	1.61	0.14
NGC 2024:Edge......	7	−1.91	0.15	4.26	0.37	2.35	0.38
LMC.....................	17	−1.70	0.17	4.37	0.44	2.71	0.40
30 Dor	5	−1.81	0.11	4.82	0.14	3.01	0.23
N160	8	−1.59	0.18	4.18	0.21	2.59	0.20
N159	4	−1.78	0.07	4.19	0.65	2.41	0.62
SMC.....................	4	...	...	...	...	2.89	0.40

[a] Number of observed positions.

[b] Average of log ($I_{C II}/I_{H_2}$). I_{H_2}, $I_{C II}$, and I_{CO} denote line intensities of H$_2$ (1, 0) S(1), [C II] 158 μm, and CO $J = 1 \rightarrow 0$.

[c] Standard deviation (a measure of how widely values are dispersed from the average value) of log ($I_{C II}/I_{H_2}$).

It may be more realistic to consider three-dimensional rather than planar clouds. In case of a three-dimensional cloud with an external far-UV field whose intensity is uniform on the surface of the cloud, the far-IR, [C II], and H$_2$ emission arise in the outer shells of the cloud, while the CO $J = 1 \rightarrow 0$ emission arises from the surface of the CO core inside the cloud. We use a geometric correction parameter, ϵ_i or ϵ_{FIR}, in equation (7) to simulate the observed intensity of a three-dimensional cloud. The spherical geometry parameter accounts for limb brightening and for the size differences between the CO, [C II], H$_2$, and far-IR emission regions in a given spherical cloud.

When examining our three-dimensional model clouds, we can eliminate the beam-filling factor, η, by dividing I_i by I_{FIR}:

$$\frac{I_i}{I_{FIR}} = \frac{\epsilon_i}{\epsilon_{FIR}} \frac{f_i(n_H, I_{UV}, \delta v_D, Z)}{2 \times 4.26 \times 10^{-4} I_{UV}}. \quad (9)$$

We will therefore divide the observed intensities by the far-IR intensity at each position as a means of removing distance-related beam-filling factor effects in our subsequent analysis of the data from the Galaxy and the Magellanic Clouds.

4.4. Relationship between I_{CO}, $I_{C II}$, and I_{H_2}

Table 8 shows the average ratios between the observed H$_2$ (1, 0) S(1), CO $J = 1 \rightarrow 0$, and C II intensities, and the
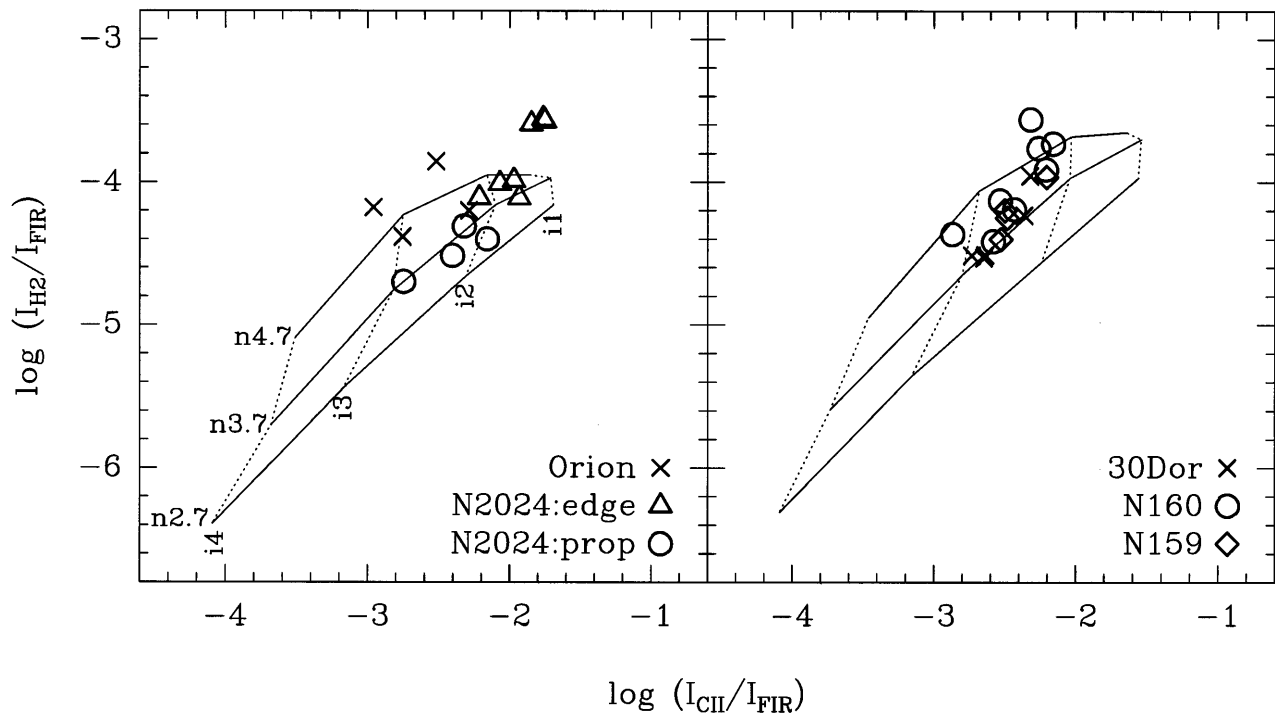

FIG. 8.—I_{H_2}/I_{FIR} vs. $I_{C II}/I_{FIR}$. Data in the left plot are from the Galactic clouds; in the right plot from the LMC. We overlay the results from the two-sided plane-parallel models (see § 5.3). We used the Galactic parameters for the model results in the left plot, and the LMC parameters in the right plot (see Table 9 for the list of parameters). In the model grids, the solid and the dotted lines connect the same n_H and the same I_{UV}, respectively. The term $n3.7$ denotes $n_H = 5 \times 10^3$ cm^{-3}, and $i3$ denotes $I_{UV} = 10^3$.
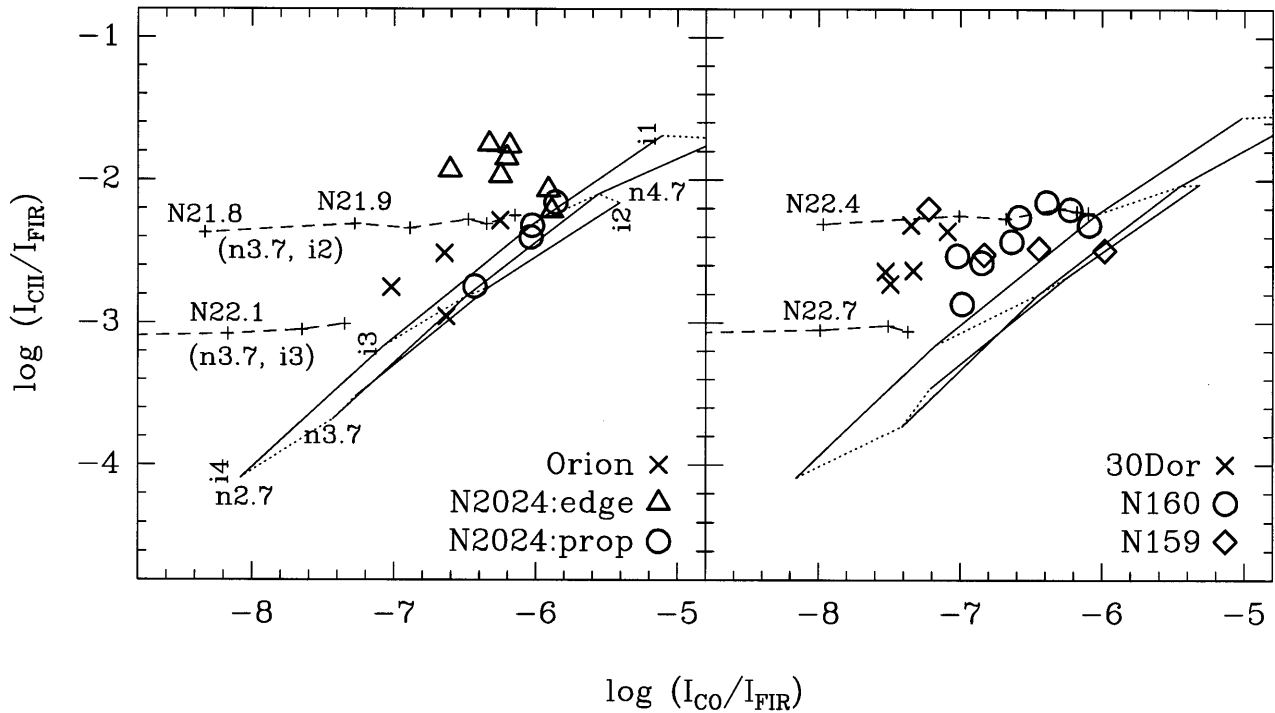
FIG. 9.—$I_{C II}/I_{FIR}$ versus I_{CO}/I_{FIR}. See Fig. 8 for explanations of the model grids of the solid lines and the dotted lines. We also plot models that include the effects of spherical geometry (*dashed lines*; see § 5.4). Dashed lines connect the spherical models with the same n_H and I_{UV} with different cloud sizes: the upper dashed line is for $n_H = 5 \times 10^3$ cm^{-3} and $I_{UV} = 10^2$; the lower line is for $n_H = 5 \times 10^3$ cm^{-3} and $I_{UV} = 10^3$. The plus sign on the dashed line marks the cloud size spaced by 0.1 in logarithmic scale. $N22.3$ denotes $N_H(2R_{cloud}) = 2n_H R_{cloud} = 10^{22.3}$ cm^{-2}. See Fig. 13 for another plot of these data.

standard deviations of the ratio distributions in the Galactic clouds and in the Magellanic Clouds.

Figures 8, 9, and 10 show plots of I_{H_2}/I_{FIR} versus $I_{C II}/I_{FIR}$, $I_{C II}/I_{FIR}$ versus I_{CO}/I_{FIR}, and I_{H_2}/I_{FIR} versus I_{CO}/I_{FIR} for the Galactic clouds and the clouds in the Magellanic Clouds.

From these figures and Table 8, the line ratios of log $(I_{H_2}/I_{C II})$ between the Galaxy and the Magellanic Clouds are in good agreement, and the ratios of log $(I_{C II}/I_{CO})$ and log (I_{H_2}/I_{CO}) in the Magellanic Clouds are slightly higher than (but in agreement with, within the standard deviations)
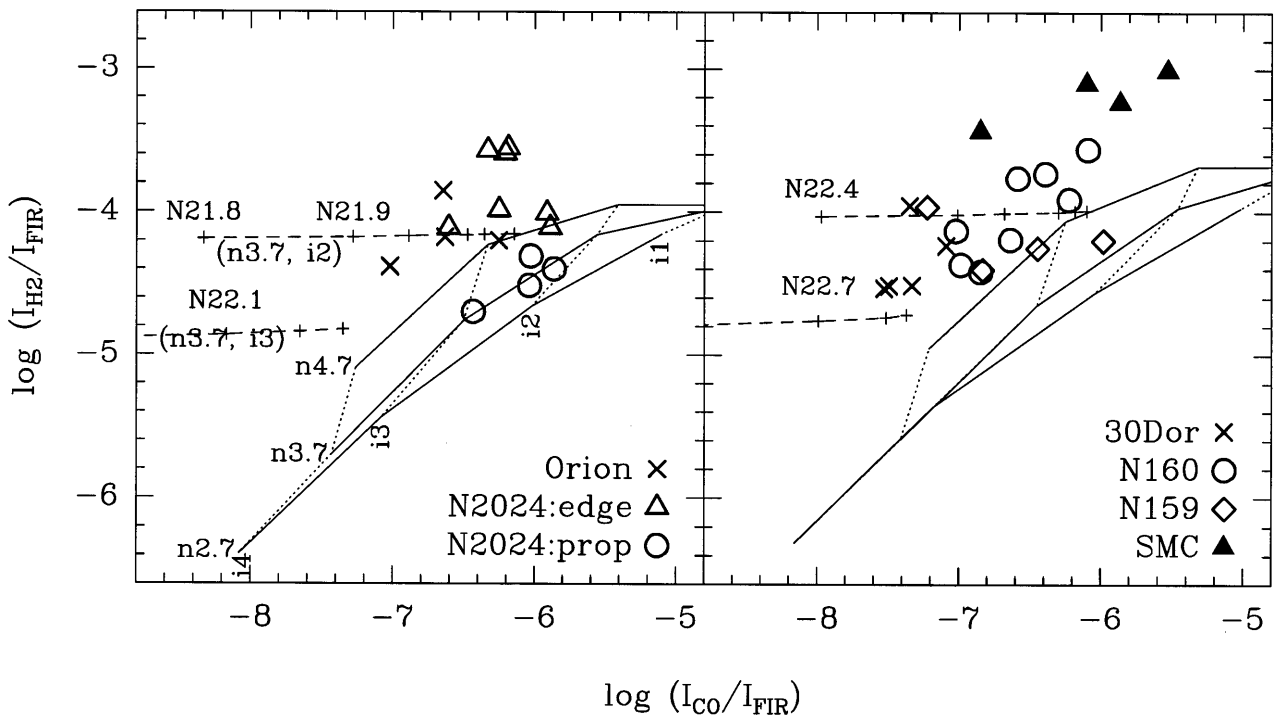

FIG. 10.—I_{H_2}/I_{FIR} vs. I_{CO}/I_{FIR}. See Figs. 8 and 9 for explanation of notations.

those in the Galaxy. Section 5 will discuss our PDR models and compare the observed data with PDR models with various input parameters.

5. MODELS

Using plane-parallel codes, the metallicity dependence of PDR structure and emergent line intensities has been calculated and discussed by several authors (Maloney & Black 1988; van Dishoeck & Black 1988b; Wolfire et al. 1989; Maloney & Wolfire 1997). The emergent intensities of the H_2 (1, 0) $S(1)$, [C II], and CO $J = 1 \rightarrow 0$ lines from PDRs depend on n_H, I_{UV}, δv_D, and Z (see § 4.3). As long as the CO $J = 1 \rightarrow 0$ line is optically thick, the resulting intensities of the CO, [C II], and H_2 (1, 0) $S(1)$ lines are not very sensitive to the metallicity. A simplified analysis can illustrate the reason for this insensitivity. In the outer part of the PDR, gas-phase carbon is in the form of C^+. When the metallicity is lowered, the number density of C^+ ions drops, but the far-UV photons penetrate deeper into the clouds because the dust-to-gas ratio is also lower. Thus, the column density of C^+ in the PDR is almost independent of the metallicity. The [C II] line is optically thin, and the intensity is proportional to the column density of C^+. The CO $J = 1 \rightarrow 0$ intensity depends much more weakly on the CO column density because the line is optically thick and most of emission arises on the surface of the CO region inside the cloud. Therefore, the CO $J = 1 \rightarrow 0$ intensity outside of very high column density cloud cores does not depend strongly on the metallicity when one considers emission from a plane-parallel slab. We will discuss the metallicity dependence of H_2 in §§ 5.2 and 5.3.

As we discussed in § 4.3, in the case of three dimensional clouds, we use the parameter ϵ_i or ϵ_{FIR} to account for effects such as limb brightening and the size differences between the outer shells, from which far-IR, [C II], and H_2 (1, 0) $S(1)$ emission arises, and the inner CO core, from which CO $J = 1 \rightarrow 0$ emission arises. The depths from the cloud surface to the C^+/C transition layer and to the H/H_2 transition layer are about inversely proportional to the dust abundance, so metal and dust abundances are more important parameters in spherical-shell PDRs than in plane-parallel models. Störzer, Stutzki, & Sternberg (1996) and Mochizuki (1996) modeled a PDR on the surface of a spherical cloud with Galactic metallicity. This section presents our own models of spherical-shell PDRs and calculates the emergent line intensities for a range of densities, UV fields, and metallicities.

5.1. Codes

We first ran a plane-parallel PDR code (van Dishoeck & Black 1986; Black & van Dishoeck 1987; van Dishoeck & Black 1988a; Jansen et al. 1995) with a range of densities ($n_H = 5 \times 10^2$, 5×10^3, and 5×10^4 cm^{-3}), UV fields ($I_{UV} = 10$, 10^2, 10^3, and 10^4), and metallicities (for the Galaxy, the LMC, and the SMC). In this code, one side of the model cloud is exposed to UV radiation, and the cloud is divided into 200 slabs, each of which is in chemical steady state. Since the code only includes inelastic collisions of H_2 within $v = 0$, the ro-vibrational level populations of H_2 are not correct at $n_H \geq 5 \times 10^4$ cm^{-3}. The PDR code calculates the gas temperature and chemical abundances in each slab. Since there is no detailed information on the grain properties in the LMC and SMC, we assume that the formation rate of H_2 on grains scales linearly with the dust abundance

(see § 5.2) and that the heating efficiencies of the grains are the same as in the Galactic case. In practice, the lower H_2 grain formation rate is accomplished in the models by decreasing the parameter y_f (Black & van Dishoeck 1987) from 1.0 to 0.25 and 0.1 in the LMC and SMC, respectively. Table 9 lists input parameters for the code.

We employ spherically symmetric cloud models to study the effects arising in three-dimensional chemical structures. The outputs (e.g., chemical abundances and kinetic temperatures) from the plane-parallel code are applied to the spherical shells of the cloud used in the radiative transfer model. We map the temperatures and abundances derived at each distance from the H II/H I interface by the plane-parallel model into the spherical radiation transfer model, ignoring any changes in the chemistry or thermal balance arising from the difference in geometry. The Monte Carlo code of Choi et al. (1995; hereafter MC) calculates the level populations of the atoms and molecules. The MC code simulates photons in a one-dimensional (spherical) cloud, and adjusts the level populations according to the result of simulations until the populations converge. We assume a purely turbulent velocity field with a Doppler velocity dispersion of 1 km s^{-1} (δv_D or half-width at $1/e$ point) with no systematic motion. Since the MC calculation includes only 40 slabs, the 200 slab plane-parallel model was smoothed in such a way as to retain a high resolution at the transition regions (Li 1997).

We use the output of the MC to calculate emission-line profiles using a virtual telescope code (Choi et al. 1995; hereafter VT). The VT code convolves the integrated emission from each spherical shell along the line of sight with a virtual telescope beam profile to simulate observations. While it would be better to examine the geometric effects using fully self-consistent models that calculate the detailed H_2 excitation, CO photodissociation, and CO and C II line intensities, our present three-step procedure should be good enough to allow us to analyze the global properties of the Galactic and LMC clouds and to establish relative trends.

5.2. Effect of H_2 Self-Shielding

Inside neutral clouds, the external far-UV field is attenuated by dust absorption, and by C and H_2 absorption. CO absorption of far-UV is negligible in the outer part of the cloud because most of the carbon is ionized. H_2 can survive in the outer parts of the cloud as a result of either self-shielding or shielding by dust. We can analyze the conditions under which H_2 self-shielding from far-UV photons is dominant over shielding by dust (adapted from Burton et

TABLE 9

INPUT PARAMETERS FOR THE PDR CODE

Object	$N_H{}^a$ (10^{22} cm^{-2})	$Z_C{}^b$	$Z_O{}^b$	$\rho_{dust}{}^c$	ζ^d (10^{-17} s^{-1})
Galaxy......	1	1	1	1	5
LMC	4	0.25	0.25	0.25	5
SMC^e	10	0.1	0.33	0.1	5

[a] H column density of the model cloud. $N_H = N(H) + 2N(H_2)$.
[b] Carbon and Oxygen abundances normalized to Galactic values, $[C]^{GAL} = 1.6 \times 10^{-4}$ and $[O]^{GAL} = 5 \times 10^{-4}$. Because the abundances are uncertain, we use simplified values in the model calculation.
[c] Dust-to-gas ratio normalized to the Galactic value, $[A_V/N_H]^{GAL} = 6.29 \times 10^{-22}$ mag cm^{-2} (Bohlin et al. 1983; Black & van Dishoeck 1987).
[d] An atomic hydrogen cosmic-ray ionizing frequency.
[e] Only for a standard model with $n_H = 5 \times 10^3$ cm^{-3} and $I_{UV} = 10^3$.

al. 1990). Within a plane-parallel cloud, the H_2 formation rate $F(x)$ at depth x measured from the surface of the cloud toward the center is

$$F(x) = n(H, x)n_H q\Re , \qquad (10)$$

where n_H is the hydrogen number density, $n_H = n(H, x) + 2n(H_2, x)$, assumed to be constant over the cloud, $n(H, x)$ and $n(H_2, x)$ are number densities at x of H atoms and H_2 molecules, respectively, $\Re$ is the value of the H_2 formation rate coefficient (a quantity that depends linearly on the dust abundance) for the Galactic dust abundance, and q is the dust abundance normalized to the Galactic value, i.e., $q^{GAL} = 1$. $\Re$ is a slowly varying function of the gas temperature ($\Re \propto T^{1/2}$), so we take an average value (3×10^{-17} cm^{-3} s^{-1}; Burton et al. 1990) for this analysis. If we assume that at the position we are considering, the dust optical depth is negligible and the H_2 absorption is governed by the square root portion of the curve of growth (Jura 1974), the far-UV field is attenuated by $N(H_2, x)^{1/2}$, where

$$N(H_2, x) = \int_0^x n(H_2, x)dx . \qquad (11)$$

The H_2 destruction rate, $D(x)$, at depth x is

$$D(x) = \frac{I_{UV} I_0 \beta}{N(H_2, x)^{1/2}} n(H_2, x) , \qquad (12)$$

where I_0 is the unshielded dissociation rate of H_2 at $I_{UV} = 1$ (7.5×10^{-11} s^{-1}; Black & van Dishoeck 1987) and β is the self-shielding parameter (4.2×10^5 cm^{-1}; Jura 1974). We can integrate the steady-state equation, $F(x) = D(x)$, over x:

$$n_H q\Re \int_0^x n(H, x)dx = I_{UV} I_0 \beta \int_0^x \frac{n(H_2, x)}{N(H_2, x)^{1/2}} dx . \qquad (13)$$

By substituting equation (11) into the above equation, we get

$$n_H q\Re N(H, x) = 2I_{UV} I_0 \beta N(H_2, x)^{1/2} . \qquad (14)$$

H_2 self-shielding is more important than dust shielding when the far-UV field attenuation by dust is still negligible,

$$\tau_{dust}(x_0) \leq \tfrac{1}{2} , \qquad (15)$$

at the point x_0, where the molecular hydrogen column density becomes equal to the atomic hydrogen column density,

$$N(H, x_0) = 2N(H_2, x_0) . \qquad (16)$$

Here $\tau_{dust}(x)$ is the optical depth of dust at $\lambda = 100$ nm. Even though the ratio of τ_{dust}/A_V depends on the chemical composition and the size distribution of the dust, the change of this ratio from the Galaxy to the LMC and the SMC is negligible compared to that of the dust-to-gas ratio; the ratios of $A_{0.1 \mu m}/A_B$ in the Galaxy, the LMC, and the SMC are 3.4, 4.1, and 5.1, respectively (Pei 1992), while A_V/N_H changes by a factor of 10 (Table 9). To simplify our analysis, we assume that the ratio of τ_{dust}/A_V is constant and that only the dust-to-gas ratio (adopted from Bohlin et al. [1983] and Black & van Dishoeck [1987]) depends on the metallicity:

$$\tau_{dust}(x) \simeq 3.0 A_V(x) \qquad (17)$$

and

$$A_V(x) = 6.29 \times 10^{-22} \rho_{dust} N_H(x) , \qquad (18)$$

where ρ_{dust} is the dust-to-gas ratio normalized to the Galactic value (see Table 9), and $N_H(x)$ is the hydrogen column density, $N_H(x) = N(H, x) + 2N(H_2, x)$. Substituting equation (16) into equation (14), we obtain the following relationship between the column density at which self-shielding becomes effective and the density, metallicity, and strength of the incident UV field:

$$N_H(x_0)^{1/2} = 2 \frac{\beta I_0}{\Re} \frac{I_{UV}}{q n_H} \simeq 2.1 \times 10^{12} \frac{I_{UV}}{q n_H} . \qquad (19)$$

From equations (15), (17), (18), and (19), we derive the conditions under which the H_2 self-shielding is dominant over shielding by dust:

$$\frac{n_H}{I_{UV}} \geq 1.3 \times 10^2 \rho_{dust}^{-1/2} , \qquad (20)$$

where we assume that the optical absorption properties and the efficiency for H_2 formation of the dust per unit H atom vary in the same way as with dust abundance, $q = \rho_{dust}$. Figure 11 shows the linear size of the C^+ region (X_{C+}) and the H_2^* region (X_{H_2*}, H_2^* denotes vibrationally excited H_2) from the PDR model results; X_{C+} and X_{H_2*} are the distances from the surface of the cloud to the inner edges of the C^+ region where $n(C^+, X_{C+}) = n(CO, X_{C+})$ and to the H_2^* region where $n(H, X_{H_2*}) = n(H_2, X_{H_2*})$, respectively.

The plot of X_{H_2*} in Figure 11 shows how H_2 self-shielding affects the depth of the H_2^* region from the surface of the cloud. Based on equation (20), the dotted lines divide the (I_{UV}, n_H, X_{H_2*}) space into a region where dust absorption is dominant and a H_2 self-shielding–dominant region. We can predict the behavior of X_{H_2*} as a function of I_{UV}, n_H, and ρ_{dust} using the relations derived in this section. When dust absorption is more important than H_2 self-shielding, the H_2^* zone ends when the far-UV field is attenuated to a fixed level, independent of the incident field. As a result, changes in I_{UV} result in a variation of τ_{dust} according to

$$I_{UV} \exp(-\tau_{dust}) = C , \qquad (21)$$

where C is a constant. Substituting equations (17) and (18) into the above equation gives

$$N_H(X_{H_2*}) \simeq 1.22 \times 10^{21} \frac{\log I_{UV} - \log C}{\rho_{dust}} , \qquad (22)$$

where $N_H(X_{H_2*})$ is the hydrogen column density at X_{H_2*}. In other words, if we increase I_{UV} by an order of magnitude, $N_H(X_{H_2*})$ increases only by an additional factor of $1.22 \times 10^{21} \rho_{dust}^{-1}$ cm^{-2}.

When H_2 self-shielding is dominant, from equation (19) we find

$$\log N_H(X_{H_2*}) \simeq 24.6 + 2 \log \left(\frac{I_{UV}}{q n_H}\right) , \qquad (23)$$

e.g., if I_{UV} decreases by an order of magnitude, $N_H(X_{H_2*})$ decreases by 2 orders of magnitude. The above equation explains why when H_2 self-shielding dominates, the depth of the H_2^* shell decreases rapidly as I_{UV} decreases or as n_H increases (see Fig. 11).

In the LMC, $(\rho_{dust}^{LMC})^{-1/2} \simeq 2.2$ (see eq. [20]), and the dotted line in Figure 11 is shifted toward lower I_{UV} by only a factor of 2.2. Even in the case of the SMC, $(\rho_{dust}^{SMC})^{-1/2} \simeq 3.2$. Variations in metal abundance, therefore, do not significantly affect the H_2 self-shielding criterion.
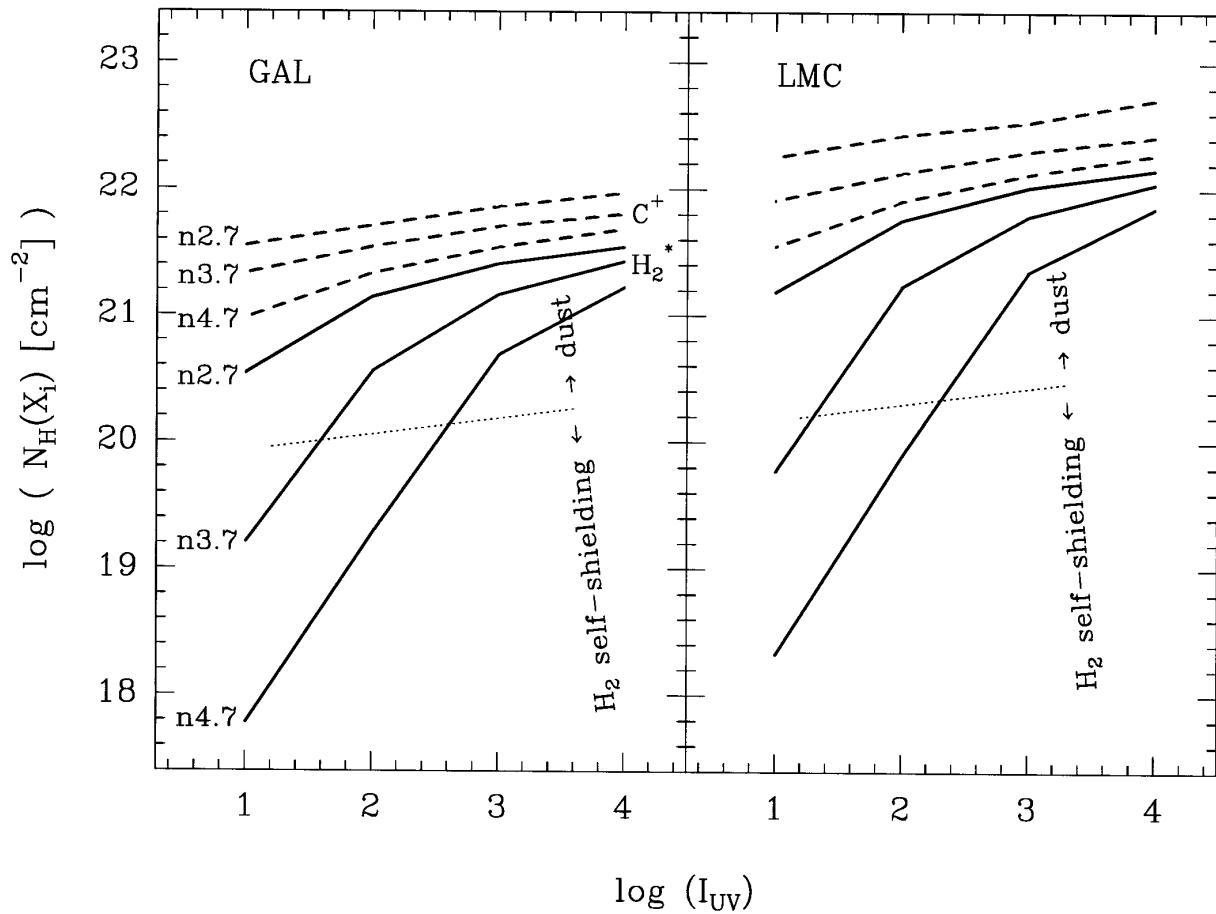
FIG. 11.—I_{UV} vs. the depths $[N_H(X) = Xn_H]$ from the surface of the cloud to the H-to-H$_2$ transition layer (where the abundance of H becomes same as that of H$_2$; *solid lines*), and to the C$^+$-to-C-to-CO transition layers (where the abundance of C$^+$ becomes same as that of CO; *dashed lines*). We changed the initial parameters, e.g., n_H, I_{UV}, and Z, for each model. n2.7 denotes $n_H = 5 \times 10^2$ cm^{-3}. At fixed density, the dashed and solid lines show the change of X_{C^+} and X_{H_2*}, respectively. The dotted line divides the (I_{UV}, n_H, X_{H_2*}) space into H$_2$ self-shielding–dominant space and dust absorption–dominant space (see eq. [20]).

5.3. Emission Intensities without Spherical Geometry Effects, ϵ

We first ran the MC and VT codes to obtain results where the spherical natures of the model clouds (e.g., limb brightening and the geometrical size differences; see § 4.3) are not important by setting the virtual telescope beam size (θ_D) much smaller than the cloud size ($2R_{cloud}$). This permits us, in effect, to obtain the line intensities from a plane-parallel cloud with a finite thickness whose front and back surfaces are exposed to external far-UV radiation. The surfaces of the cloud are perpendicular to the line of sight. These models are equivalent to setting $\eta = 1$ and $\epsilon_i = 1$ in equation (7): $I_i = f_i$. The resulting [C II] intensity is from both the front and back surfaces, because the [C II] line emission is nearly optically thin (Stacey et al. 1991). The CO $J = 1 \to 0$ line is optically thick, so the resulting CO emission comes predominantly from the front surface.

The VT code does not calculate the ro-vibrational lines of H$_2$. We derive the H$_2$ (1, 0) S(1) emission from the H$_2^*$ column density, $N(H_2^*)$, which results from the plane-parallel PDR model. The electronically excited H$_2$ molecules relax radiatively to the ground electronic state and then cascade through the vibrational energy levels by emitting ro-vibrational lines. In this process, the H$_2$ line ratios are insensitive to n_H and I_{UV}, and we can use a constant conversion factor between $N(H_2^*)$ and H$_2$ (1, 0) S(1) intensity

(Black & van Dishoeck 1987):

$$f_{H_2}^{front} = 2.67 \times 10^{-21} N(H_2^*) \text{ ergs s}^{-1} \text{ cm}^{-2} \text{ sr}^{-1} , \quad (24)$$

where $f_{H_2}^{front}$ is the intensity from the front surface of the cloud.

While the ro-vibrational lines of H$_2$ are optically thin, the emission from the back surface, $f_{H_2}^{back}$, is affected by the extinction, A_K, through the cloud itself. Using $A_K = 0.112A_V$ (Rieke & Lebofsky 1985) and equation (18), we estimate the observed intensity from the back surface as

$$\log (f_{H_2}^{back}) = \log (f_{H_2}^{front}) - \frac{\rho_{dust} N_H}{3.5 \times 10^{22} \text{ cm}^{-2}} . \quad (25)$$

As we will discuss in § 5.4, the cloud size (in units of hydrogen column density N_H) has a lower limit, necessary to keep the CO molecules from being dissociated completely in an intense far-UV field ($I_{UV} > 10^3$). Figure 13 shows that $\rho_{dust} N_H$ should be larger than 2×10^{22} cm^{-2}; therefore,

$$f_{H_2}^{back} < 0.3 f_{H_2}^{front} . \quad (26)$$

We will neglect the H$_2$ emission from the back side of the cloud in the following discussion, and take $f_{H_2} \simeq f_{H_2}^{front}$. In some cases, there may be a bit of additional flux from the back side penetrating through the thinner parts of the cloud.

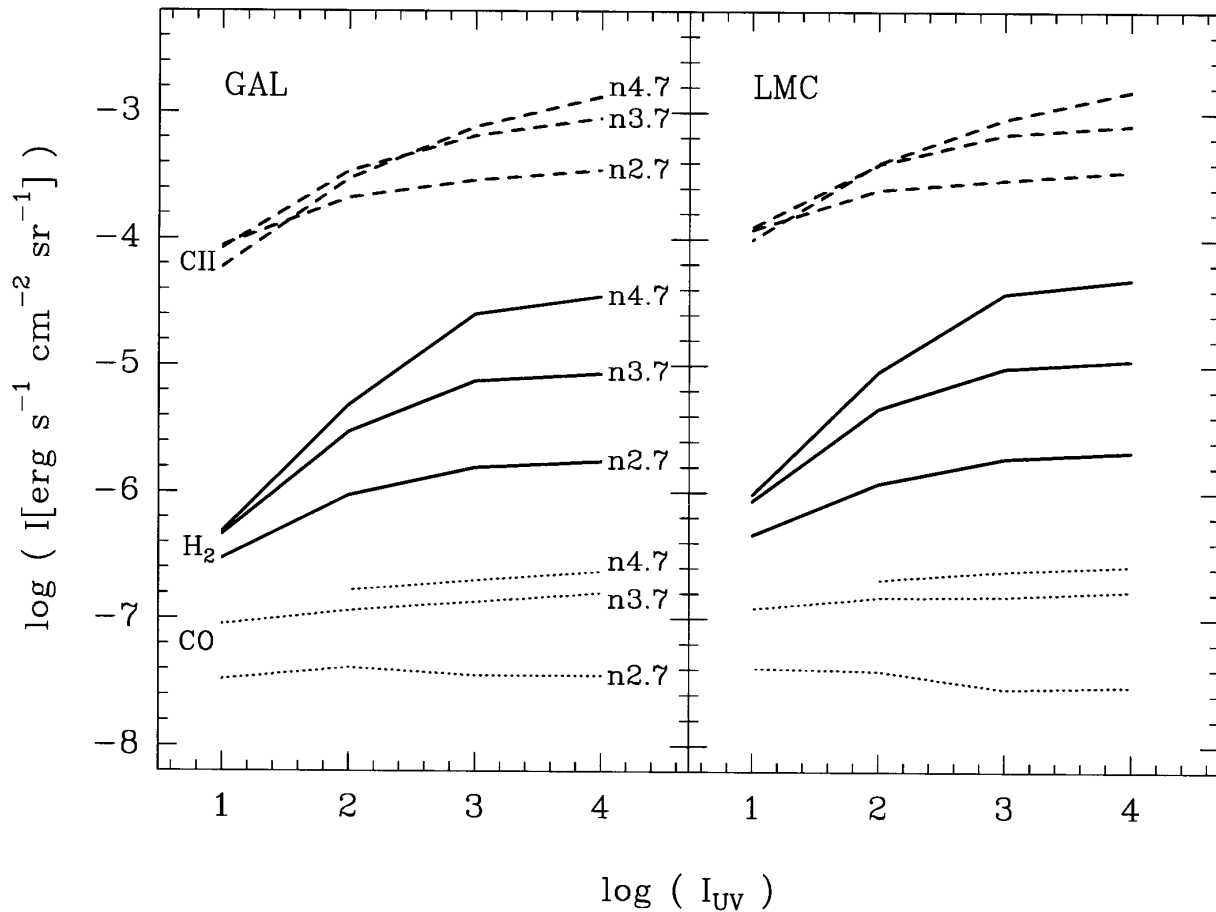FIG. 12.—I_{UV} vs. [C II] (dashed line), H_2 (1, 0) $S(1)$ (solid line), and CO $J = 1 \to 0$ (dotted line) emission line intensities at fixed density. We assume that $\eta = 1$ and that the intensities do not include the geometry effect ($\epsilon_i = 1$): $I_i = f_i(n_{\mathrm{H}}, I_{\mathrm{UV}}, Z)$.

Figure 12 shows the [C II], H_2 (1, 0) $S(1)$, and CO $J = 1 \to 0$ emission intensities from the PDR code and the MC/VT code for the two-sided planar clouds. When dust absorption dominates (eq. [20]), the H_2 intensity increases as n_{H} increases. On the other hand, when H_2 self-shielding dominates, the H_2 intensity increases as I_{UV} increases. In the LMC model (Fig. 12, right panel), the H_2 intensity is enhanced by a factor of $10^{0.1}$–$10^{0.3}$ over the intensity in the Galactic model with the same n_{H} and I_{UV}. The enhancement is mainly due to the different H_2 self-shielding criteria in the Galactic model and in the LMC model.

5.4. Model Emission Intensities Including the Effects of Spherical Geometry

In order to understand the effect of limb brightening and of differences in the physical sizes of the C^+, H_2^*, and CO zones in spherical clouds of varying metallicity, we ran the VT code with the virtual telescope beam size (θ_{ED}) set to match the cloud size ($2R_{\mathrm{cloud}}$). The resulting intensities are equivalent to setting $\eta = 1$ in equation (7): $I_i = \epsilon_i f_i$. In Figure 13, we plot the model values of $I_{\mathrm{C\,II}}$, $I_{\mathrm{H_2}}$, and I_{CO} versus cloud size. In Figures 6, 9, and 10, we overlay the results on the observed data. $I_{\mathrm{C\,II}}$ and I_{CO} are obtained directly from the VT code, and the far-IR continuum emission and $I_{\mathrm{H_2}}$ are from equation (7), with ϵ_{FIR} and $\epsilon_{\mathrm{H_2}}$ derived as follows.

As we discussed in § 4.3, the effects of spherical geometry include both limb brightening and size differences between the different emission regions in the cloud. The far-IR emis-

sion has a very low optical depth, and the H_2 (1, 0) $S(1)$ emission is optically thin. The far-IR and H_2 emission regions lie on the surface of the cloud and fill the telescope beam. We can analyze the spherical geometry effects for optically thin lines by projecting the three-dimensional emission shell onto a two-dimensional emission disk:

$$\epsilon_i = \frac{1}{2X_i \pi R_{\mathrm{cloud}}^2} \int_{R_{\mathrm{cloud}} - X_i}^{R_{\mathrm{cloud}}} 4\pi R^2 \, dR$$

$$= 2 - 2\frac{X_i}{R_{\mathrm{cloud}}} + \frac{2}{3}\left(\frac{X_i}{R_{\mathrm{cloud}}}\right)^2, \qquad (27)$$

where X_i is the depth from the cloud surface to the transition regions, e.g., X_{C^+} and $X_{H_2^*}$, defined in § 5.2, and R_{cloud} is the radius of the cloud. In the above equation, we assume that $n(H_2^*)/n_{\mathrm{H}}$ and $n(C^+)/n_{\mathrm{H}}$ are constant in the corresponding shells. For the far-IR emission, if we consider that the incident far-UV energy is conserved as the output far-IR energy (see eq. [4]), we can write

$$\epsilon_{\mathrm{FIR}} = \frac{4\pi R_{\mathrm{cloud}}^2}{2\pi R_{\mathrm{cloud}}^2} = 2 . \qquad (28)$$

We use equation (27) to obtain $\epsilon_{\mathrm{H_2}}$, and equation (28) to obtain $\epsilon_{\mathrm{FIR}} = 2$.

The CO line arises on the surface of the CO core. Because external UV radiation provides most of the heating, the gas temperature gradient is positive, $dT/dR > 0$ ($R = 0$ at the cloud center). As we observe an optically thick line, the edge of the projected CO disk has a higher brightness tem-
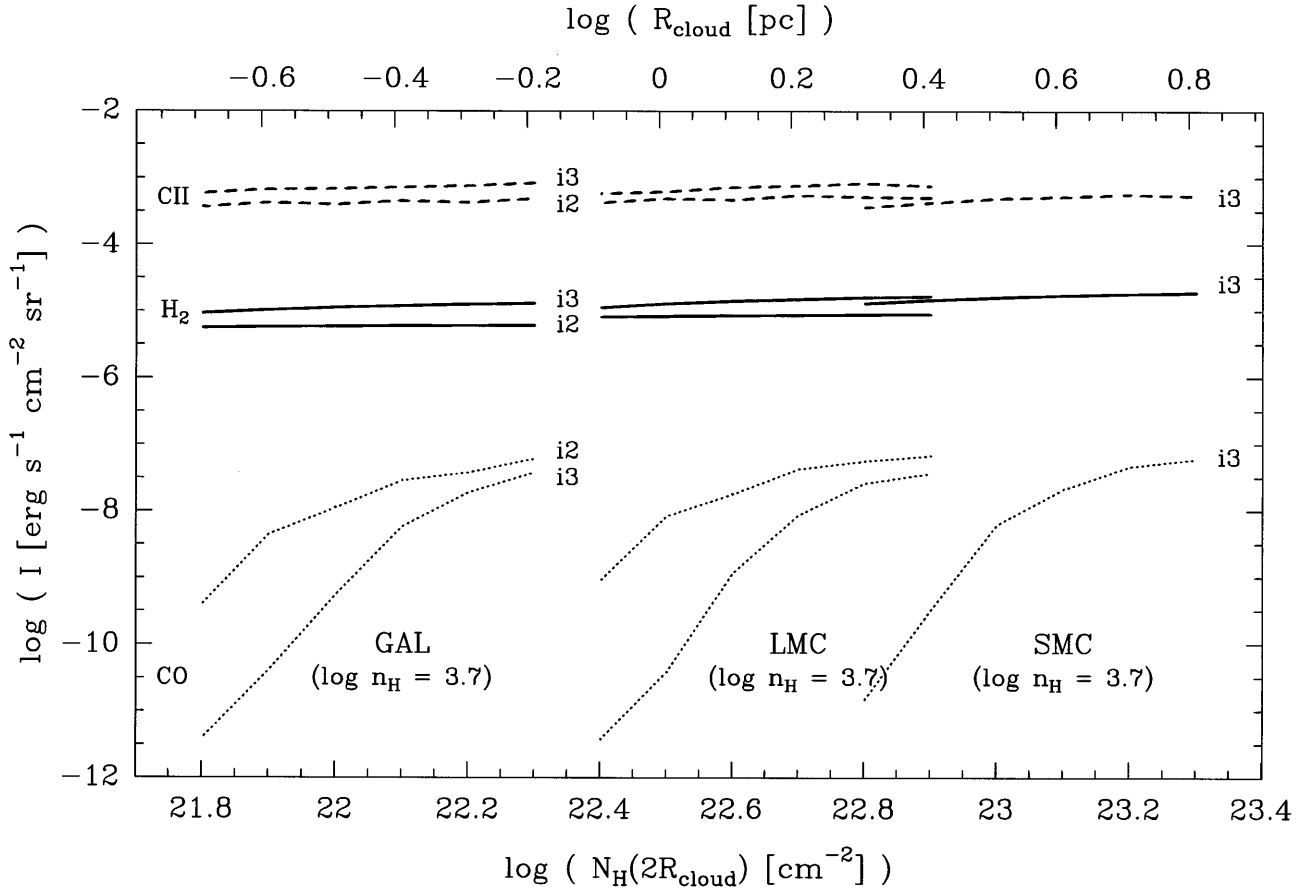
$$\log (\ R_{cloud}\ [pc]\ )$$

FIG. 13.—[C II] (*dashed line*), H_2 (1, 0) $S(1)$ (*solid line*), and CO $J = 1 \rightarrow 0$ (*dotted line*) line intensities vs. R_{cloud} at $n_H = 5 \times 10^3$ cm^{-2}, $I_{UV} = 10^2$, 10^3. $I2$ and $i3$ denote $I_{UV} = 10^2$ and 10^3, respectively. We assume that $\eta = 1$ and that the intensities include the effect of spherical geometry: $I_i = \epsilon_i f_i(n_H, I_{UV}, Z)$. $I_{C II}$ and I_{CO} are directly from the VT code, and I_{H_2} is from $\epsilon_{H_2} f_{H_2}$ via eqs. (24) and (27). We plot only the range of N_H where significant changes take place in each model. The upper axis shows the cloud radius in pc, and the lower axis shows the central column density of the spherical cloud in cm^{-2}: $N_H(2R_{cloud}) = 2R_{cloud} n_H$. Note that $N_H(X)$ in Fig. 11 is $X n_H$, where $X_{C+} = R_{cloud} - R_{CO}$.

perature than the center, and we see limb brightening. On the other hand, the size of the CO core (R_{CO}) is smaller than the cloud size (R_{cloud}), which is affected by I_{UV} and n_H. When R_{cloud} is larger than X_{C+} and I_{CO} is optically thick,

$$\epsilon_{CO} \simeq \left(\frac{R_{CO}}{R_{cloud}}\right)^2 = \left(1 - \frac{X_{C+}}{R_{cloud}}\right)^2. \qquad (29)$$

When we compare the spherical cloud models to plane-parallel models, the change in the CO core size (R_{CO}) is more significant than the limb-brightening effect. We plot the CO intensity (by setting $\eta = 1$) resulting from the numerical code in dotted lines in Figure 13. This method also takes into account any additional effect of opacity variations on the local CO emissivity. As $R_{CO} \rightarrow 0$, the resulting I_{CO} decreases rapidly.

5.5. Applying the Model to the Data

As we discussed in §§ 5.3 and 5.4, the observed far-IR, [C II], and H_2 (1, 0) $S(1)$ line intensities depend almost exclusively on n_H and I_{UV}, while the observed CO $J = 1 \rightarrow 0$ line intensity depends on n_H, I_{UV}, Z, and R_{cloud}. In this section, we apply the model results to the data and estimate n_H, I_{UV}, and R_{cloud} in the regions we observed.

5.5.1. I_{H_2} versus $I_{C II}$

In Table 8, the standard deviations of the observed $\log (I_{H_2}/I_{C II})$ are smaller than those of other ratios (0.1–0.2

vs. 0.2–0.4) because the values of $f_{C II}$ and f_{H_2} depend similarly on n_H and I_{UV} (see Fig. 12), and in the case of spherical clouds, the [C II] and H_2 intensities are not very sensitive to variations in cloud size, i.e., $\frac{2}{3} < (\epsilon_{C II}, \epsilon_{H_2}) < 2$ (see eq. [29] and Fig. 13).

In Figure 8, most of the data from NGC 2024 are within the model grids at $3.2 < \log n_H < 4.2$ and $1.5 < \log I_{UV} < 3$. There are positions (at $\Delta\alpha = -17'$, $-16'$, and $-15'$) in NGC 2024, however, where the I_{H_2} intensities lie at least a factor of 2.5 above the model grids. At these positions, the clouds may be small enough to be transparent for H_2 emission from the back side of the cloud (see eq. [25]). Based on our experience with other positions, it is extremely unlikely that the H_2 level populations at these positions are thermalized by effects present in high-density PDR's ($n_H > 5 \times 10^4$ cm^{-3}) or by shocks (see § 3.4). The ratios of $\log (I_{H_2}/I_{C II})$ in Orion are larger than those in NGC 2024. The Orion data in Figure 8 lie slightly below and slightly above models for $\log n_H = 4.7$, implying that the gas density in Orion is higher than that in NGC 2024.

The mean ratios of $\log (I_{H_2}/I_{C II})$ in 30 Doradus, N159, and N160 are similar, suggesting that the observed clouds in the LMC have similar densities and that collisional deexcitation does not affect the H_2 level populations (see Table 8). In Figure 8, most of the data for the LMC match models in the range of $3.7 < \log n_H < 4.7$ and $2 < \log I_{UV} < 3$.

By comparing the observed data and the model results in Figure 8, we measure the median density and far-UV field

for each source. With this derived n_H and I_{UV}, we found the C^+ region depth, X_{C+}, using Figure 11. The values of n_H, I_{UV}, and X_{C+} determined in this way are listed in Table 10.

5.5.2. $I_{C\,II}$ versus I_{CO}

Both cloud size differences and metallicity differences affect the observed $I_{C\,II}/I_{CO}$ and I_{H_2}/I_{CO} ratios. For the clouds in NGC 2024, the results of Jaffe et al. (1994) implied that the size of the clouds (R_{cloud}) in the western edge zone is smaller than those in the cloud proper zone (see § 4.1), while the C^+ region depth in the cloud, X_{C+}, is not much different. As we discussed in § 5.4, for a given n_H and I_{UV}, I_{CO} is proportional to ϵ_{CO}. In the LMC, the dust-to-gas ratio, ρ_{dust}^{LMC}, is lower than in the Galaxy by a factor of ~ 4, and the far-UV radiation penetrates deeper into the clouds (see Fig. 14):

$$\frac{X_{C+}^{LMC}}{X_{C+}^{GAL}} \simeq \frac{\rho_{dust}^{GAL}}{\rho_{dust}^{LMC}} \simeq 4 . \qquad (30)$$

If we assume that the cloud sizes in the Galaxy and in the LMC are same, then ϵ_{CO}^{LMC} is less than ϵ_{CO}^{GAL}. If $\epsilon_{CO}^{LMC} \simeq \epsilon_{CO}^{GAL}$, the cloud size in the LMC must be larger than the cloud size in the Galaxy (see Fig. 14).

The $I_{C\,II}/I_{CO}$ ratio is also affected by the strength of the UV field. Mochizuki et al. (1994) compared the $\log (I_{C\,II}/I_{CO})$ ratios in the LMC with the ratios in the Galactic plane. Their log ratio in the LMC, 4.4 ± 0.3, agrees well with our ratio in 30 Doradus, N160, and N159 (4.2–4.8, see Table 8); however, their ratio in the Galactic plane, 3.1 ± 0.5, is much smaller than the ratio in Orion and NGC 2024 (3.7–4.3, see Table 8). We argue that the Galactic plane at $-12° < l < +26°$ has a different physical environment from active star formation regions such as Orion and NGC 2024. Most of the $I_{60\,\mu m}/I_{100\,\mu m}$ ratios at the positions in the Galactic plane are between 0.2 and 0.3 (see Fig. 2 of Nakagawa et al. 1995). Applying these ratios to equations (2), (4), and (6) (see also eq. [32]), we can estimate that the
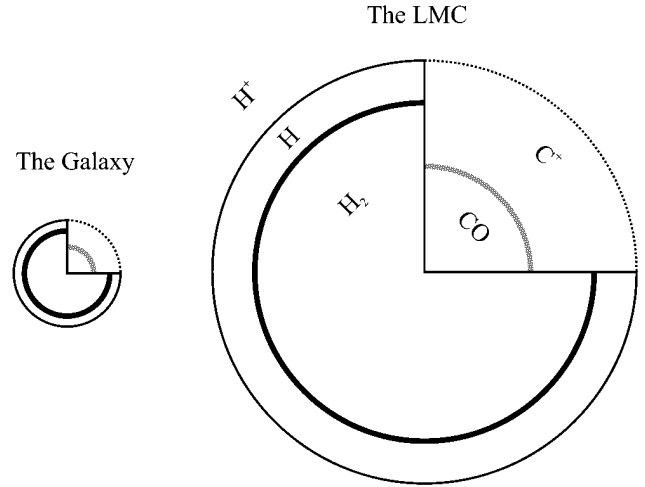

FIG. 14.—Schematic of chemical structures and sizes of typical clouds in the Galaxy and the LMC. Assuming that the far-UV field (I_{UV}) and the gas density (n_H) are same in the clouds in both galaxies, the cloud size in the LMC is 4 times bigger than that in the Galaxy, i.e., the typical size of the star-forming clouds is inversely proportional to the metallicity of the galaxy.

far-UV fields in the Galactic plane are in the range of $1.5 < \log I_{UV} < 1.7$. The far-UV field is, therefore, much lower than toward the positions we observed in Orion and NGC 2024 ($1.9 < \log I_{UV} < 3.2$). Our model results in Figure 12 show that at $\log I_{UV} = 1.6$ and $\log n_H = 3.7$, the $\log (I_{C\,II}/I_{CO})$ ratio is 3.2, which agrees with the observed value of the Galactic plane in Mochizuki et al. (1994). On the other hand, the far-UV fields in 30 Doradus, N160, and N159 are very high ($2.0 < \log I_{UV} < 3.8$). Even the extended regions in the LMC for which Mochizuki et al. (1994) measured the $\log (I_{C\,II}/I_{CO})$ ratio show higher far-UV fields ($1.8 < \log I_{UV} < 2.7$, derived from the $I_{60\,\mu m}/I_{100\,\mu m}$ ratios) than those in the Galactic plane. The more intense far-UV

TABLE 10
DERIVED CLOUD COLUMN DENSITIES

Object	ρ_{dust} [a]	N [b]	$\log n_H$	$\log I_{UV}$	$N(X_{C+})$ [c]	ϵ_{CO} [d]	$N_H(2R_{cloud})$ [e] (10^{22} cm^{-2})
Galaxy	1	>15					
Galactic Plane [f]	...	...	(3.7)	1.6	0.29	>0.63	>1.4
Orion		4	4.7	2.5	0.27	0.44	1.6
NGC 2024:Prop		4	3.7	2.5	0.45	>0.63	>4.3
NGC 2024:Edge		7	3.7	1.8	0.32	0.083	0.89
LMC	0.25	17					
30 Dor		5	4.0	2.7	1.5	0.048	3.9
N160		8	4.2	2.7	1.5	0.17	5.0
N159(−1.5, 0)		1	4.1	2.7	1.5	>0.63	>15
N159(+1, +1)		1	3.9	2.7	1.7	0.36	8.4
N159(0, 0)		1	3.7	2.7	1.8	0.15	5.8
N159(0, +3)		1	4.1	2.3	1.2	0.063	3.2
SMC [f]	0.1	4	(3.7)	2.6	4.5	>0.1	>13
IC 10 [f,g]	0.2	2					
Position A		1	(3.7)	2.7	2.2	0.3	9.9
Position B		1	(3.7)	2.6	2.0	0.1	5.8

[a] Dust-to-gas ratio normalized to the Galactic value.
[b] Number of observed positions.
[c] Depth from the surface of the cloud to the C^+-to-C-CO transition layers.
[d] Parameter of the spherical geometry effect.
[e] Central column density of the spherical cloud. Note that $N_H(2R_{cloud}) = 2R_{cloud} n_H$, and $R_{cloud} = X_{C+} + R_{CO}$.
[f] We assume that $\log n_H = 3.7$. We derive $\log I_{UV}$ from IRAS far-IR data. See the text for details.
[g] We adopt results from Madden et al. (1997).

fields, e.g., in Orion, NGC 2024, 30 Doradus, N160, and N159, dissociate more CO molecules and have deeper C^+ regions, X_{C^+}, in equation (29); therefore, the $I_{C\,II}/I_{CO}$ ratio becomes larger.

Figure 9 plots the observed data, $I_{C\,II}/I_{FIR}$ versus I_{CO}/I_{FIR}, and overlays the results from the planar cloud models and the spherical cloud models. For the spherical cloud models, the tick marks along the dashed lines mark the positions in the space of models with different column densities, $N_H(2R_{cloud})$. The locus of each model comes from the value of $I_{C\,II} = \epsilon_{C\,II} f_{C\,II}$ and $I_{CO} = \epsilon_{CO} f_{CO}$ determined for that column density. The solid and dotted lines show the results of the planar cloud model ($I_{C\,II} = f_{C\,II}$ and $I_{CO} = f_{CO}$, respectively). Only the data from the cloud proper zone in NGC 2024 are within the planar cloud model space, and most of the observed data deviate systematically from the model results toward lower I_{CO}/I_{FIR} or higher $I_{C\,II}/I_{FIR}$. The models do not include spherical geometry effects (see § 5.3), and equation (27) implies that the observed $I_{C\,II}$ data should not be significantly affected by going from plane-parallel to spherical geometry. Therefore, the offset of observed points from the models on the $I_{C\,II}$ versus I_{CO} plot in Figure 9 is solely a result of the effect of spherical geometry on the observed I_{CO} emission (ϵ_{CO}). Given the observed value of $I_{C\,II}/I_{FIR}$, we measured how much the observed I_{CO}/I_{FIR} is shifted from the point expected from the models for a given density and far-UV intensity on the model grids in Figure 9,

$$\Delta \log (I_{CO}/I_{FIR}) = \log \epsilon_{CO} . \qquad (31)$$

Applying the measured X_{C^+} and ϵ_{CO} to equation (29), we derived the column densities through the clouds [$N_H(2R_{cloud})$ in Table 10] under the assumption that the clouds are spherical. For the data from the cloud proper zone in NGC 2024, we use the uncertainty in the observations to set the lower limit, i.e., $\epsilon_{CO} \geq 10^{-0.2}$.

Madden et al. (1997) also estimated ϵ_{CO} for the nearby irregular galaxy, IC 10, using far-IR, [C II], and CO $J = 1 \rightarrow 0$ data. In Table 10 we list the adopted values of I_{UV} and ϵ_{CO} at positions A and B in IC 10. Using the dust-to-gas ratio of IC 10, $\rho_{dust}^{IC10} \simeq 0.2$, and the PDR models, we estimate $N(C^+)$ and then $N_H(2R_{cloud})$.

5.5.3. I_{H_2} versus I_{CO}

Models indicate that, like $I_{C\,II}$, I_{H_2} is not affected strongly by changing from planar to spherical geometry. Therefore, the similar offset of the data from models in Figure 10 is probably a result of the inappropriateness of using the plane-parallel models to predict I_{CO}. As with the data in Figure 9, only the data from the cloud proper zone in NGC 2024 are within the model space, and most of the observed data deviate systematically leftward from the model results.

The data from the SMC, which are not available in Figure 9, also deviate toward lower $\log (I_{CO}/I_{FIR})$ or higher $\log (I_{H_2}/I_{FIR})$ from the LMC model results, if we assume that the SMC models without spherical geometry effects are not very different from the LMC models. In the SMC, the observed H_2 emission could be higher than the model results as a result of the unreddened H_2 emission from the back side of the cloud. Because [C II] data are not available and the H_2 data are not certain, we cannot measure ϵ_{CO}^{SMC} from the I_{H_2} versus I_{CO} plane. We can still estimate a lower limit on the column density of clouds in the SMC, assuming $\epsilon_{CO} \geq 10^{-1}$. Applying the dust temperature of $10^{1.65}$ K from $IRAS$ 60 $\mu m/100$ μm ratios (see Fig. 7) to equations (4)

and (6),

$$\log I_{UV} = -5.65 + 5 \log T_{dust} , \qquad (32)$$

we obtain a far-UV field (I_{UV}) of $10^{2.6}$ at the observed positions in the SMC. Assuming $\log n_H = 3.7$, we get $N_H(X_{C^+}^{SMC}) = 4.5 \times 10^{22}$ cm^{-2}. Therefore, the central column density (N_H) of the clouds in the SMC should be at least 1.3×10^{23} cm^{-2} (see Table 10).

5.6. Cloud Column Densities in Galactic and Magellanic Complexes

We estimate cloud column densities in the molecular complexes in the Galaxy and in the Magellanic Clouds. We first derive n_H and I_{UV} by comparing the observed data and the model results in the I_{H_2}/I_{FIR} versus $I_{C\,II}/I_{FIR}$ plot (Fig. 8). We take a median value of the data in each object, except in N159, where we consider each position separately. Using the values of n_H and I_{UV} derived from Figure 8, we get X_{C^+}, the depth from the surface of the cloud to the C^+-to-C-to-CO transition layer, in Figure 11. We also get ϵ_{CO}, the parameter that accounts for spherical geometry, by comparing the data and models in Figure 9. When we do not have C^+ or H_2 data, we assume that $\log n_H = 3.7$, and estimate I_{UV} from the dust color temperature using $I_{60\,\mu m}/I_{100\,\mu m}$ and equations (2) and (32). We finally derive the central column densities of clouds using equation (29) and list them in Table 10 (see also Fig. 15). Note that the column densities derived in this way are a measure of the
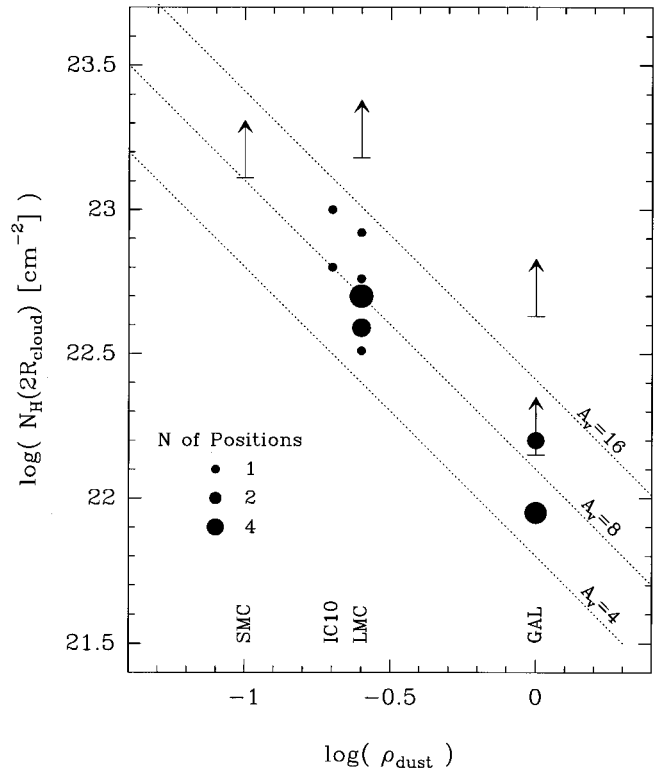

FIG. 15.—Central column density of spherical cloud vs. dust-to-gas ratio from the Galaxy, the LMC, the SMC, and IC 10 (see also Table 10). Note that the cloud size is presented by the hydrogen column density for a given density, $n_H = 5 \times 10^3$ cm^{-3}: $N_H(2R_{cloud}) = 2R_{cloud} n_H$, and ρ_{dust} is normalized to the Galactic value. The area of the filled circle represents the number of observed positions. The arrow shows the lower limit. For comparison with the theory of photoionization-regulated star formation, we overlay the constant optical depths at $A_V = 4$, 8, and 16 mag.

number of molecules between the H II/H boundary and the cloud center, not of the overall column density through the GMC complexes.

The cloud column density measured in the western edge zone in NGC 2024 is at least a factor of 5 smaller than the column density measured in the cloud proper zone in NGC 2024. At the four data positions in N159, the variations of n_H and I_{UV} are not significant, e.g., $3.7 < \log n_H < 4.1$ and $2.3 < \log I_{UV} < 2.7$; however, the I_{CO} intensities change by a factor of $10^{1.2}$, indicating that the column density varies by more than a factor of 5 within the N159 region. The cloud sizes represented by the hydrogen column density for a given density $n_H = 5 \times 10^3$ cm^{-3} in the LMC ($N_H^{LMC} = 3 - 15 \times 10^{22}$ cm^{-2}), the SMC ($>1.3 \times 10^{23}$), and IC 10 (6–10 $\times 10^{22}$ cm^{-2}) are bigger than those in the Galaxy ($N_H^{GAL} = 1$–4×10^{22} cm^{-2}).

5.7. Column Density and Metallicity

Table 10 and Figures 14 and 15 show that the column density and (for constant density) cloud size depend roughly linearly on metallicity, and therefore the visual extinction through clouds is constant as one goes from the Galaxy to the LMC and SMC.

McKee (1989) presented a theory of *photoionization-regulated star formation* (see also Bertoldi & McKee 1996). According to his theory, the rate of low-mass star formation is governed by ambipolar diffusion in magnetically supported clouds, and the ionization of gas is mostly by far-UV photons. He suggested that the mean extinction of molecular clouds in dynamical equilibrium is in the range of $A_V = 4$–8 mag. Using equation (18), the range of extinction corresponds to

$$0.64 \times 10^{22} \text{ cm}^{-2} < \rho_{dust} N_H < 1.3 \times 10^{22} \text{ cm}^{-2} . \quad (33)$$

This range of column density roughly agrees with the empirical values of Galactic GMCs using I_{CO} and the virial theorem, $N_H = 4$–8 $\times 10^{22}$ cm^{-2} (Scoville et al. 1987; Solomon et al. 1987). In regions with higher incident UV fields, the equilibrium range should move to higher column density. Our results from the Galaxy, the LMC, the SMC, and IC 10 are also within $A_V = 4$–16 mag, and agree with the theory to within a factor of 2 for the range of observed incident fields.

6. CONCLUSIONS

We observed H$_2$ (1, 0) $S(1)$, (2, 1) $S(1)$, and (5, 3) $O(3)$ lines from the Magellanic Clouds and detected emission even in regions where CO had not been seen during the ESO-SEST Key Program, implying that H$_2$ is present in these regions. With deeper CO observations, we also detected weak (0.5–5 K km s^{-1}) CO emission in PDRs where the previous ESO-SEST Program did not detect CO $J = 1 \to 0$. We conclude that in all regions where we could detect H$_2$, CO is not completely dissociated, and that the CO $J = 1 \to 0$ emission is still optically thick in the Magellanic Clouds. Our observations may have consequences for studies using CO to trace molecular mass.

Our spherical-shell cloud model demonstrates the effects of limb brightening and differences in the physical sizes of the C$^+$, H$_2^*$, and CO zones on the observed line strengths. The H$_2$, [C II], and CO line intensities from the plane-parallel cloud model are not very sensitive to the metallicity. When geometric effects are taken into account using spherical models, the H$_2$, and [C II] line intensities normalized to the far-IR intensity are also not very sensitive to the metallicity; however, the CO intensity is proportional to the surface area of the CO core. As we decrease the cloud size (or total column density, N_H), the CO intensity normalized to the far-IR intensity decreases.

We compiled data of H$_2$ (1, 0) $S(1)$, CO $J = 1 \to 0$, [C II], and far-IR in the star formation regions in the Magellanic Clouds and in the Galaxy, and compared these with simulated line intensities from a plane-parallel cloud. The data in the I_{H_2}/I_{FIR} versus $I_{C II}/I_{FIR}$ plot agree with the model results, and show no significant difference between the Magellanic Clouds and the Galaxy. We use the I_{H_2}/I_{FIR} versus $I_{C II}/I_{FIR}$ plot to estimate n_H and I_{UV} at the positions we observed. In the $I_{C II}/I_{FIR}$ versus I_{CO}/I_{FIR} and I_{H_2}/I_{FIR} versus I_{CO}/I_{FIR} plots, the data from the western edge zone in NGC 2024 and from the Magellanic Clouds are shifted to the lower I_{CO} than the model results, which can be explained as an effect of spherical geometry. We measured the amount of the effect, and used the result to derive the column density through the clouds.

On galaxy scales, the derived average column density and therefore size of the clouds appears to increase as the metallicity of the galaxy decreases. Our observational result, that the mean extinction of clouds is constant and independent of their metallicity, is consistent with the idea that photoionization may play a role in regulating star formation.

REFERENCES

Anthony-Twarog, B. J. 1982, AJ, 87, 1213
Arimoto, N., Sofue, Y., & Tsujimoto, T. 1996, PASJ, 48, 275
Aumann, H. H., Fowler, J. W., & Melnyk, M. 1990, AJ, 99, 1674
Bertoldi, F., & McKee, C. F. 1996, in Amazing Light: A Volume Dedicated to C. H. Townes on his 80th Birthday, ed. R. Y. Chiao (New York: Springer)
Black, J. H., & van Dishoeck, E. F. 1987, ApJ, 322, 412
Bloemen, J. B. G. M., et al. 1986, A&A, 154, 25
Bohlin, R. C., Hill, J. K., Jenkins, E. B., Savage, B. D., Snow, T. P., Jr., Spitzer, L., Jr., & York, D. G. 1983, ApJS, 51, 277
Booth, R. S. 1993, in Second European Meeting on the Magellanic Clouds, New Aspects of Magellanic Cloud Research, ed. B. Baschek, G. Klare, & J. Lequeux (Berlin: Springer), 26

Burton, M. G., Brand, P. W. J. L., Geballe, T. R., & Webster, A. S. 1989, MNRAS, 236, 409
Burton, M. G., Hollenbach, D. J., & Tielens, A. G. G. M. 1990, ApJ, 365, 620
Choi, M., Evans, N. J., II, Gregersen, E. M., & Wang, Y. 1995, ApJ, 448, 742
Cohen, R. S., Dame, T. M., Garay, G., Montani, J., Rubio, M., & Thaddeus, P. 1988, ApJ, 331, L95
Digel, S., et al. 1997, in IAU Symp. 170, CO: Twenty-Five Years of Millimeter-Wave Spectroscopy, ed. W. B. Latter et al. (Dordrecht: Kluwer), 22
Draine, B. T. 1978, ApJS, 36, 595
Draine, B. T., & Bertoldi, F. 1996, ApJ, 468, 269

Draine, B. T., & Lee, H. M. 1984, ApJ, 285, 89
Dufour, R. J. 1984, in IAU Symp. 108, Structure and Evolution of the Magellanic Clouds, ed. S. van den Bergh & K. S. de Boer (Dordrecht: Reidel), 353
Greve, A., van Genderen, A. M., & Laval, A. 1990, A&AS, 85, 895
Habing, H. J. 1968, Bull. Astron. Inst. Netherlands, 19, 421
Helou, G., Khan, I. R., Malek, L., & Boehmer, L. 1988, ApJS, 68, 151
Heydari-Malayeri, M., & Testor, G. 1985, A&A, 144, 98
Hollenbach, D. J., Takahashi, T., & Tielens, A. G. G. M. 1991, ApJ, 377, 192
Israel, F. P. 1988, in Millimetre and Submillimetre Astronomy, ed. R. D. Wolstencroft & W. B. Burton (Dordrecht: Kluwer), 281
Israel, F. P., de Graauw, Th., van de Stadt, H., & de Vries, C. P. 1986, ApJ, 303, 186
Israel, F. P., & Koornneef, J. 1988, A&A, 190, 21
————. 1992, A&A, 250, 475
Israel, F. P., & Maloney, P. R. 1993, in Second European Meeting on the Magellanic Clouds, New Aspects of Magellanic Cloud Research, ed. B. Baschek, G. Klare, & J. Lequeux (Berlin: Springer), 44
Israel, F. P., Maloney, P. R., Geis, N., Hermann, F., Madden, S. C., Poglitsch, A., & Stacey, G. J. 1996, ApJ, 465, 738
Jaffe, D. T., Zhou, S., Howe, J. E., Herrmann, F., Madden, S. C., Poglitsch, A., van der Werf, P. P., & Stacey, G. J. 1994, ApJ, 436, 203
Jansen, D. J., van Dishoeck, E. F., Black, J. H., Spaans, M., & Sosin, C. 1995, A&A, 302, 223
Jefferys, W. H. 1990, Biometrika, 77, 597
Johansson, L. E. B., et al. 1998, A&A, 331, 857
Johansson, L. E. B., Olofsson, H., Hjalmarson, Å., Gredel, R., & Black, J. H. 1994, A&A, 291, 89
Jura, M. 1974, ApJ, 191, 375
Kawara, K., Nishida, M., & Taniguchi, Y. 1988, PASP, 100, 458
Koornneef, J. 1984, in IAU Symp. 108, Structure and Evolution of the Magellanic Clouds, ed. S. van den Bergh & K. S. de Boer (Dordrecht: Reidel), 333
Koornneef, J., & Israel, F. P. 1985, ApJ, 291, 156
Krabbe, A., Storey, J., Rotaciuc, V., Drapatz, S., & Genzel, R. 1991, in IAU Symp. 148, The Magellanic Clouds, ed. R. Haynes & D. Milne (Dordrecht: Kluwer), 205
Lee, M. G. 1991, in IAU Symp. 148, The Magellanic Clouds, ed. R. Haynes & D. Milne (Dordrecht: Kluwer), 207
Lequeux, J., Le Bourlot, J., Pineau des Forêts, G., Roueff, E., Boulanger, F., & Rubio, M. 1994, A&A, 292, 371
Li, W. 1997, Ph.D. thesis, Univ. Texas, Austin
Luhman, M. L., & Jaffe, D. T. 1996, ApJ, 463, 191
Luhman, M. L., Jaffe, D. T., Keller, L. D., & Pak, S. 1994, ApJ, 436, L185
————. 1995, PASP, 107, 184
Luhman, M. L., Jaffe, D. T., Sternberg, A., Herrmann, F., & Poglitsch, A. 1997, ApJ, 482, 298
Madden, S. C., Poglitsch, A., Geis, N., Stacey, G. J., & Townes, C. H. 1997, ApJ, 483, 200
Maloney, P., & Black, J. H. 1988, ApJ, 325, 389
Maloney, P., & Wolfire, M. G. 1997, in IAU Symp. 170, CO: Twenty-Five Years of Millimeter-Wave Spectroscopy, ed. W. B. Latter et al. (Dordrecht: Kluwer), 299
Mangum, J. G. 1993, PASP, 105, 117
McKee, C. F. 1989, ApJ, 345, 782
Mochizuki, K. 1996, Ph.D. thesis, Univ. Tokyo
Mochizuki, K., et al. 1994, ApJ, 430, L37
Nakagawa, T., Doi, Y., Yui, Y. Y., Okuda, H., Mochizuki, K., Shibai, H., Nishimura, T., & Low, F. 1995, ApJ, 455, L35
Pei, Y. C. 1992, ApJ, 395, 130
Poglitsch, A., Krabbe, A., Madden, S. C., Nikola, T., Geis, N., Johansson, L. E. B., Stacey, G. J., & Sternberg, A. 1995, ApJ, 454, 293
Oliva, E., & Origlia, L. 1992, A&A, 254, 466
Richter, M. J., Graham, J. R., & Wright, G. S. 1995, ApJ, 454, 277
Rieke, G. H., & Lebofsky, M. J. 1985, ApJ, 288, 618
Rubio, M., et al. 1993, A&A, 271, 1
Schloerb, F. P., & Loren, R. B. 1982, in Ann. NY Acad. Sci., 395, Symposium on the Orion Nebula to Honor Henry Draper, ed. A. E. Glassgold, P. J. Huggins, & E. L. Schucking, 32
Scoville, N. Z., Yun, M. S., Clemens, D. P., Sanders, D. B., & Waller, W. H. 1987, ApJS, 63, 821
Solomon, P. M., Rivolo, A. R., Barrett, J., & Yahil, A. 1987, ApJ, 319, 730
Spaans, M., Tielens, A. G. G. M., van Dishoeck, E. F., & Bakes, E. L. O. 1994, ApJ, 437, 270
Stacey, G. J., Jaffe, D. T., Geis, N., Genzel, R., Harris, A. I., Poglitsch, A., Stutzki, J., & Townes, C. H. 1993, ApJ, 404, 219
Stacey, G. J., Townes, C. H., Poglitsch, A., Madden, S. C., Jackson, J. M., Herrmann, F., Genzel, R., & Geis, N. 1991, ApJ, 382, L37
Sternberg, A., & Dalgarno, A. 1989, ApJ, 338, 197
Störzer, H., Stutzki, J., & Sternberg, A. 1996, A&A, 310, 592
Taylor, C., Kobulnicky, H., & Skillman, E. 1996, BAAS, 189, 122.01
Tielens, A. G. G. M., & Hollenbach, D. 1985, ApJ, 291, 722
————. 1997, ARA&A, in press
van Dishoeck, E. F., & Black, J. H. 1986, ApJS, 62, 109
————. 1988a, ApJ, 334, 771
————. 1988b, in Molecular Clouds in the Milky Way and External Galaxies, ed. R. L. Dickman, R. L. Snell, & J. S. Young (New York: Springer), 168
Westerlund, B. E. 1990, A&A Rev., 2, 29
Wilson, C. D. 1995, ApJ, 448, L97
Wolfire, W. G., Hollenbach, D., & Tielens, A. G. G. M. 1989, ApJ, 344, 770